An efficient matrix-free preconditioned conjugate gradient based multigrid method for phase field modeling of fracture in heterogeneous materials from 3D images

Xiaodong Liu, Julien Réthoré, Antonius Adrianus Lubrecht

▶ **To cite this version:**

Xiaodong Liu, Julien Réthoré, Antonius Adrianus Lubrecht. An efficient matrix-free preconditioned conjugate gradient based multigrid method for phase field modeling of fracture in heterogeneous materials from 3D images. Computer Methods in Applied Mechanics and Engineering, 2022, 388, 10.1016/j.cma.2021.114266 . hal-03381620

HAL Id: hal-03381620
https://hal.science/hal-03381620

Submitted on 17 Oct 2021

HAL is a multi-disciplinary open access archive for the deposit and dissemination of scientific research documents, whether they are published or not. The documents may come from teaching and research institutions in France or abroad, or from public or private research centers.

L'archive ouverte pluridisciplinaire **HAL**, est destinée au dépôt et à la diffusion de documents scientifiques de niveau recherche, publiés ou non, émanant des établissements d'enseignement et de recherche français ou étrangers, des laboratoires publics ou privés.

Distributed under a Creative Commons Attribution - NonCommercial 4.0 International License

An efficient matrix-free preconditioned conjugate gradient based multigrid method for phase field modeling of fracture in heterogeneous materials from 3D images

Xiaodong Liu*[1], Julien Réthoré[1], and Antonius Adrianus Lubrecht[2]

[1]Research Institute in Civil Engineering and Mechanics (GeM), CNRS UMR6183, École Centrale de Nantes, 1 rue de la Noë, 44321 Nantes Cedex 3, France
[2]Univ Lyon, INSA-Lyon, CNRS UMR5259, LaMCoS, F-69621, France

13 October, 2021

Abstract

In this paper, we present a new and efficient strategy to perform 3D computational fracture modeling from computed tomography (CT) images. The image-based fracture modeling creates a new way to more accurately predict fracture in realistic structures. However, it is currently complex and expensive to perform such simulations. In this work, we propose to use a matrix-free type preconditioned conjugate gradient solver based multigrid method to achieve the fastest numerical performance for phase field modeling of fracture. Several specific methods are investigated to enhance the robustness and to improve the efficiency of the proposed strategy. An automatic load control strategy to control crack propagation is investigated. High performance computing is applied using a hybrid MPI/OpenMP strategy. With all of the proposed procedures, the phase field modeling of fracture can be performed in the real 3D microstructure of heterogeneous materials using tomographic images.

Keywords— Preconditioned conjugate gradient based multigrid method – Phase field fracture modeling – Heterogeneous material – Image-based simulation

1 Introduction

Industrial materials, *e.g.* composite materials, biological materials, architectured materials, become more and more complex both on components and structures. The complexity of these heterogeneous materials can improve their durability. But it leads to many engineering problems, *e.g.* failure, which is due to the limited comprehension of these materials. The most common failure mode of engineering materials and structures is fracture, which can sometimes have fearful consequences, *e.g.* the fracture of a bridge. Researchers pay, therefore, close attention to the prevention of crack induced failure in engineering designs. Numerical modeling of fracture can help researchers to understand and predict failure of cracked structures, *e.g.* cast iron, composite

*Corresponding author: xiaodong.liu@ec-nantes.fr

materials, human bones, concrete, for which full-scale experiments are too expensive and even impracticable.

However, modeling fracture in these complex materials is very difficult. One of the reasons is related to the real microstructure of these highly heterogeneous materials. Fortunately, experimental techniques such as X-ray tomography [1] reveal the real microstructure of these heterogeneous materials. It gives us the opportunity to analyze micro/macro interactions. Meanwhile, it confirms that there are large differences between real and theoretical (ideal) microstructures, *e.g.* many defects can be found in the microstructure of cast iron presented in [2] and the microstructure of fiber reinforced composite laminate illustrated in [3]. The subject of this work is to perform image-based fracture modeling using real microstructures of heterogeneous materials.

Besides the complexity of highly heterogeneous materials, the fracture modeling is itself complex for various reasons. Firstly, the crack is usually very thin compared to the structural dimension. Numerically, it can create large discontinuities with traditional methods, *e.g.* finite element methods. Secondly, fracture is an irreversible process, it should not heal itself. Time-dependent constraints are therefore introduced when solving such a problem. At the same time, fracture nucleation and branching can lead to more difficulties. The phase field modeling is one of the most widely used and developed damage model due to advantages such as straightforward modeling of complex crack patterns and crack branching. The variational phase-field based approach was first introduced in [4] based on [5], in which Griffith's model ([6]) was represented by an energy minimization problem. [4] then proposed a smooth function to deal with the sharp discontinuous problem in the phase field fracture modeling. Now the phase field modeling has become very popular in the last decades. Many papers can be found both on extensions and applications of this model *e.g.* [7, 8, 9, 10, 11, 12, 13, 14, 15].

Many publications can be found on phase field fracture modeling, even for 3D models, *e.g.* [16, 7, 17, 18, 11, 13, 12], . However, few 3D works can be found for simulations using real microsctructures of materials, *e.g.* [18]. On one hand, this is due to the complexity of real microstructure. It can create many numerical difficulties and one has to handle meshing problems due to this complexity. On the other hand, the phase field modeling is usually solved by the traditional finite element approach. One of the limitations of the standard finite element method is its high cost due to memory requirement and computational time. Several works ([19, 20, 13]) propose an adaptive mesh refinement to alleviate this bottleneck. Nevertheless, it is still difficult to perform phase field fracture modeling from real 3D images. [7] is the first paper performed image-based phase field modeling. However, they just investigated a 2D real structure, their 3D modeling is performed on a theoretical (perfect) model. Meanwhile, the cost of their simulation is very high, *e.g.*, about 10 days for an ideal 3D model. Later, image-based phase field simulations and comparisons with *in-situ* experiments are presented by [17]. Highly heterogeneous image-based phase field simulations are illustrated in [18].

Based on these backgrounds and our previous work presented in [21] and [22], we propose to use a matrix free type solver to reduce memory requirement and to improve the parallel performance. This allows us to perform phase field modeling at a large scale. However, the matrix-free type solver is usually very slow to achieve convergence. We propose to apply the multigrid method to accelerate the convergence speed, which has already shown its usefulness in [21, 22] for thermal and elastic problems with billions of elements. Briefly, a matrix-free type solver based multigrid algorithm is presented in this paper to perform image-based phase field modeling of fracture in heterogeneous materials at the microscopic scale.

However, one of the limitations of multigrid methods is its ability to handle large jumps, *e.g.* high heterogeneity and rough solutions [23]. The adaptive nature of conjugate gradient can compensate for the shortcomings of the basic smoothing procedure in multigrid algorithms [23]. The combination of PCG methods and multigrid algorithms has been developed by researchers since the 1980's. [24] and [25] proposed to use the multigrid method as a preconditioner of conjugate gradient methods, which is the so-called MGCG method. [26] generalized their work

10 years later. A parallel version can be found in [27]. Applications to large scale problems were solved by the MGCG in [28]. The application of MGCG methods on mixed finite element methods was investigated in [29]. On the other hand, [23] proposed to use the PCG iterator as a smoother for multigrid algorithms, which is the so-called PCGMG method. [30] combined the MGCG method and the PCGMG method to achieve a good efficiency for elasticity problems. The ability to avoid the locking effect of multigrid methods using conjugate gradient solvers was confirmed by [30]. We therefore propose to use the PCGMG method to perform the image-based phase field modeling in heterogeneous materials. This choice was made for several reasons: (1), the Jacobi iterator based multigrid method can lead to divergence when solving the mechanical part in phase field models due to the presence of cracks, which leads to huge discontinuities; (2), replacing the Jacobi smoother by a PCG iterator does not require a amount of work in terms of implementation based on our previous work; (3), a good parallel performance can therefore be ensured with minimum modifications.

The outline of this paper is the following: Section 2 briefly presents the framework of the staggered phase field modeling. Section 3 introduces the implementation of the proposed preconditioned conjugate based multigrid algorithms by using a finite element discretization. The convergence performance analysis is employed in Section 4. Several improvements are also proposed for problems with large variations in this section. The validation of the overall program and its applications are illustrated in Section 5. The snap-back behavior during the phase field modeling is also presented in this section. An automatic load-control strategy for adjusting the displacement increment is investigated for applications in this section. Conclusions are presented at the end of this paper.

2 Problem statement

Assuming domain $\Omega \subset \mathcal{R}^D$ describes a cracked solid, with its boundary $\partial\Omega$ and D the space dimension. Let Γ be the crack in Ω as presented in Figure 1a for a $D = 2$ case.

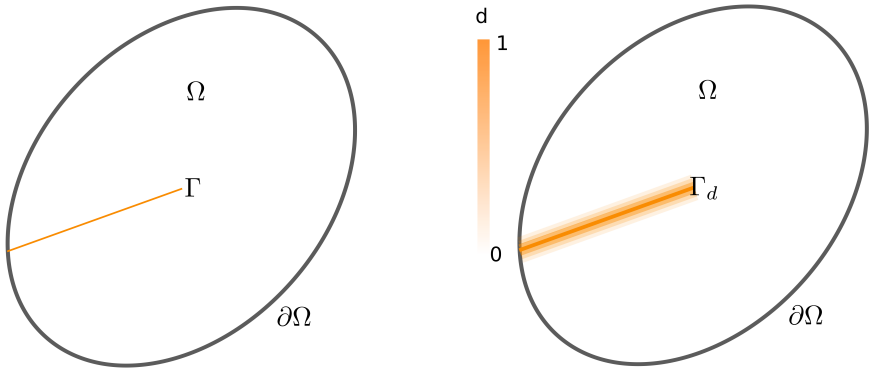

(a) Sharp crack (b) Smeared crack

Figure 1: Crack topology approximation in a $D = 2$ case

According to [31, 6] and [5], the energy equilibrium in the cracked domain Ω can be presented as:

$$\mathcal{E}(\boldsymbol{u}, \Gamma) = \mathcal{E}_u(\boldsymbol{u}, \Gamma) + \mathcal{E}_s(\Gamma) = \int_\Omega W_u\left(\boldsymbol{\epsilon}(\boldsymbol{u})\right) d\Omega + g_c \mathcal{X}^{D-1} \tag{1}$$

where $\mathcal{E}_u(\boldsymbol{u}, \Gamma)$ is the elastic energy which can be described as the integral of strain energy density $W_u\left(\boldsymbol{\epsilon}(\boldsymbol{u})\right)$ in the entire domain. $\boldsymbol{\epsilon} = \frac{1}{2}(\nabla \boldsymbol{u} + \nabla \boldsymbol{u}^T)$ denotes the strain with the displacement $\boldsymbol{u}$. $\mathcal{E}_s(\Gamma)$ denotes the energy required to create the crack in Ω according to the Griffith criterion in [31, 6]. It can be expressed as the product of the Hausdorff surface measure $\mathcal{X}^{D-1}$ and the

fracture toughness g_c which represents the energy required to create a unit cracked surface for $D = 3$.

2.1 Phase field modeling

However, to solve a fracture problem with a sharp crack (Figure 1a) numerically, is complex. Meanwhile, crack initiation, branching or more generally topological changes of the crack are extremely difficult to model. [4] therefore proposed a smooth function instead of a sharp crack. The formulation to represent the diffuse crack illustrated in Figure 1b, is presented for example in [16]. It reads:

$$\begin{cases} d - \ell_c^2 \Delta d = 0 & \text{in } \Omega \\ d(\boldsymbol{x}) = 1 & \text{on } \Gamma \\ \nabla d(\boldsymbol{x}) \cdot \boldsymbol{n} = 0 & \text{on } \partial\Omega \end{cases} \tag{2}$$

where $d(\boldsymbol{x})$ describes the states of materials, which is defined as a crack phase field in [16], with $x \in \Omega$. Δ is the Laplacian operator. ℓ_c represents the actual diffuse crack thickness. Equation (2) is the Euler-Lagrange equation associated with the variational problem:

$$d = Arg\left\{\inf \Gamma_d\right\} \qquad d \in \{d | d(\boldsymbol{x}) = 1 \text{ on } \Gamma \quad \forall \boldsymbol{x} \in \Gamma\}$$

where:

$$\Gamma_d = \int_\Omega \gamma(d, \nabla d)\, d\Omega \tag{3}$$

represents the crack surface functional for a 3D case. $\gamma(d, \nabla d)$ is the crack density function per unit volume, defined in this work by:

$$\gamma(d, \nabla d) = \frac{1}{2\ell_c} d^2 + \frac{\ell_c}{2} (\nabla d)^2 \tag{4}$$

In the phase field modeling, $\mathcal{X}^{D-1}$ denotes the crack surface functional Γ_d. Substituting equation (1) and (3), we obtain:

$$\mathcal{E}(\boldsymbol{u}, \Gamma) = \int_\Omega W_u\left(\boldsymbol{\epsilon}(\boldsymbol{u})\right)\, d\Omega + g_c \int_\Omega \gamma(d, \nabla d)\, d\Omega = \int_\Omega W\, d\Omega \tag{5}$$

where the free energy W reads:

$$W = W_u\left(\boldsymbol{\epsilon}(\boldsymbol{u})\right) + \frac{g_c}{2\ell_c} d^2 + \frac{g_c \ell_c}{2} (\nabla d)^2 \tag{6}$$

To correctly compute $W_u\left(\boldsymbol{\epsilon}(\boldsymbol{u})\right)$, the unilateral contact formulation presented in [32] is adopted in this work. It reads:

$$W_u\left(\boldsymbol{\epsilon}(\boldsymbol{u})\right) = \begin{cases} g_k(d) \left\{ \frac{1}{2} K \left[tr(\boldsymbol{\epsilon})\right]^2 + G \boldsymbol{\epsilon}_{dev} : \boldsymbol{\epsilon}_{dev} \right\} & tr(\boldsymbol{\epsilon}) \geq 0 \\ \frac{1}{2} K \left[tr(\boldsymbol{\epsilon})\right]^2 + g_k(d) G \boldsymbol{\epsilon}_{dev} : \boldsymbol{\epsilon}_{dev} & tr(\boldsymbol{\epsilon}) < 0 \end{cases} \tag{7}$$

where K is the bulk modulus and G denotes the shear modulus. $\boldsymbol{\epsilon}_{dev} = \boldsymbol{\varepsilon} - \frac{1}{3} tr(\boldsymbol{\varepsilon}) \boldsymbol{I}$ is the deviatoric part of strain tensor. $tr(\boldsymbol{\epsilon})$ is the trace of strain tensor. Ψ^+ and Ψ^- represent the positive and negative part of energy, respectively. It reads:

$$\Psi^+ = \begin{cases} \frac{1}{2} K \left(tr(\boldsymbol{\epsilon})\right)^2 + G \boldsymbol{\epsilon}_{dev} : \boldsymbol{\epsilon}_{dev} & tr(\boldsymbol{\epsilon}) \geq 0 \\ G \boldsymbol{\epsilon}_{dev} : \boldsymbol{\epsilon}_{dev} & tr(\boldsymbol{\epsilon}) < 0 \end{cases} \tag{8}$$

and

$$\Psi^- = \begin{cases} 0 & tr(\boldsymbol{\epsilon}) \geq 0 \\ \frac{1}{2} K tr(\boldsymbol{\epsilon})^2 & tr(\boldsymbol{\epsilon}) < 0 \end{cases} \tag{9}$$

The degradation function $g_k(d)$ is chosen according to [8], which reads:

$$g_k(d) = (1-k)g(d) + k \tag{10}$$

where

$$g(d) = (1-d)^2$$

The small parameter k is to maintain the well-posedness of the partially broken system as proposed in [16].

The stress $\boldsymbol{\sigma}$ can therefore be expressed as:

$$\boldsymbol{\sigma} = K_d tr(\boldsymbol{\varepsilon})\boldsymbol{I} + 2G_d\left(\boldsymbol{\varepsilon} - \frac{1}{3}tr(\boldsymbol{\varepsilon})\right) \tag{11}$$

where if $\Psi^+ \geq \Psi^-$

$$K_d = \begin{cases} [(1-k)g(d)+k]\cdot K & tr(\boldsymbol{\epsilon}) \geq 0 \\ K & tr(\boldsymbol{\epsilon}) < 0 \end{cases} \tag{12}$$

and

$$G_d = [(1-k)g(d)+k]\cdot G \tag{13}$$

while if $\Psi^+ < \Psi^-$, d is set to 0 and the initial elastic properties K, G are recovered. The governing equations to determine the displacement field in Ω can be written as:

$$\begin{cases} d = 0 & \Psi^+ < \Psi^- \\ \nabla \cdot \boldsymbol{\sigma} = \boldsymbol{0} & \text{in } \Omega \\ \boldsymbol{u} = \boldsymbol{U}_0 & \text{on } \partial\Omega_D \\ \boldsymbol{\sigma}\cdot\boldsymbol{n} = \boldsymbol{f}_{ext} & \text{on } \partial\Omega_N \end{cases} \tag{14}$$

where $\boldsymbol{U}_0$ is the prescribed displacement and $\boldsymbol{f}_{ext}$ is the surface forces. The Dirichlet and Neumann boundary conditions are prescribed on $\partial\Omega_D$ and $\partial\Omega_N$, respectively.

According to the second law of thermodynamics, we have:

$$\boldsymbol{\sigma} : \dot{\boldsymbol{\epsilon}} - \dot{W} \geq 0 \tag{15}$$

Substituting $\boldsymbol{\sigma} = \partial W/\partial\epsilon$, we obtain:

$$-\frac{\partial W}{\partial d}\dot{d} \geq 0 \tag{16}$$

As the crack propagation is irreversible, $\dot{d} \geq 0$. We obtain:

$$-\frac{\partial W}{\partial d} = 0 \tag{17}$$

Considering $k \approx 0$, we can therefore obtain the governing equations to compute the phase field d:

$$\begin{cases} 2(1-d)\mathcal{H} - \frac{g_c}{\ell_c}(d - l^2\Delta d) = 0 & \text{in } \Omega \\ d(\boldsymbol{x}) = 1 & \text{on } \Gamma \\ \nabla d(\boldsymbol{x})\cdot\boldsymbol{n} = 0 & \text{on } \partial\Omega \end{cases} \tag{18}$$

where $\mathcal{H}$ represents the maximum of elastic energy over history as proposed in [16]. It reads:

$$\mathcal{H}(\boldsymbol{x}, t) = max\left(\Psi^+(\boldsymbol{\epsilon}(\boldsymbol{x}, t)) - \Psi_c\right) \tag{19}$$

with $\Psi_c = \frac{g_c}{2\ell_c}$. It is a threshold that we prescribed according to [8]. It means the damage will only appear when $\mathcal{H} \geq \Psi_c$.

The overall staggered phase field modeling can be presented as follows:

Loop on time step t

- Compute displacement $\boldsymbol{u}$ with equation (14)
- Calculate $\mathcal{H}$ with equation (19)
- Obtain d with equation (18)

end loop

3 Implementation

To perform image-based phase field modeling in heterogeneous materials, we use the strategy proposed in our previous papers [21, 22] using a finite element based multigrid method. However, we will present a more efficient solver instead of the simple Jacobi iterator proposed in [21, 22].

3.1 Finite element discretization

The procedure of finite element discretization for equation (14) was proposed in [22]. In this paper, we present a detailed finite element discretization for solving equation (18). We still propose to associate one elementary node per image voxel. The chosen element type is 8-node linear hexahedron.

The weak form of equation (18) is:

$$\int_\Omega \left(2\mathcal{H} + \frac{g_c}{\ell_c}\right) dd^* \, d\Omega - \int_\Omega g_c \ell_c \Delta d d^* \, d\Omega = \int_\Omega 2\mathcal{H} d^* \, d\Omega \tag{20}$$

where d^* is the test function. Applying partial integration:

$$\int_\Omega \left(2\mathcal{H} + \frac{g_c}{\ell_c}\right) dd^* \, d\Omega + \int_\Omega g_c \ell_c \nabla d \nabla d^* \, d\Omega - \int_{\partial\Omega} \nabla d \cdot \boldsymbol{n} d^* \, dS = \int_\Omega 2\mathcal{H} d^* \, d\Omega \tag{21}$$

with $\int_{\partial\Omega} \nabla d \cdot \boldsymbol{n} d^* \, dS = 0$. Equation (21) is therefore:

$$\int_\Omega \left(2\mathcal{H} + \frac{g_c}{\ell_c}\right) dd^* \, d\Omega + \int_\Omega g_c \ell_c \nabla d \nabla d^* \, d\Omega = \int_\Omega 2\mathcal{H} d^* \, d\Omega \tag{22}$$

which can be written in the vector form:

$$\boldsymbol{F}_L^d = \boldsymbol{F}_R^d \tag{23}$$

with

$$\begin{cases} \boldsymbol{F}_L^d = & \int_\Omega \left(2\mathcal{H} + \frac{g_c}{\ell_c}\right) dd^* \, d\Omega + \int_\Omega g_c \ell_c \nabla d \nabla d^* \, d\Omega \\ \boldsymbol{F}_R^d = & \int_\Omega 2\mathcal{H} d^* \, d\Omega \end{cases} \tag{24}$$

Applying finite element discretization:

$$d \approx \sum_1^N \phi_i \hat{d}_i$$

where ϕ_i denotes the shape function. N is the number of unknowns. i denotes the node id. $\hat{d}_i$ is thus the approximation of d at node i. Supposing:

$$d^* = \phi_i$$

Equation (24) for elementary node j of one 8-node cubic element becomes:

$$\begin{cases} F_{Lj}^{d} = & \sum_{e} \sum_{g=1}^{8} \sum_{i=1}^{8} \left[\left(2\mathcal{H} + \frac{g_c}{\ell_c} \right) \phi_i \phi_j \hat{d}_i + g_c \ell_c \nabla \phi_i \nabla \phi_j \hat{d}_i \right] \\ F_{Rj}^{d} = & \sum_{e} \sum_{g=1}^{8} 2\mathcal{H} \phi_j \end{cases} \tag{25}$$

where $\sum_e$ is the sum over neighboring elements, $\sum_g$ is the sum over Gauss integration points, $\sum_i$ is the sum over shape function.

3.2 Preconditioned conjugate gradient

In the previous part, we proposed to compute the left and the right hand of equation (23) at each elementary node, instead of using typical assembled system matrices, because a matrix-free type solver is applied to reduce memory requirements as presented in [22]. However, the Jacobi solver used in [21] and [22] can not handle huge discontinuities, *e.g.* divergence occurs for a spherical inclusion mechanical problem with a material property contrast of 1000 (Figure 5). In the mechanical part of phase field modeling, huge discontinuities, *e.g.* contrast larger than 10^5, can be found due to the presence of cracks. Instead of using the Jacobi solver, we therefore propose to use the preconditioned conjugate gradient (PCG) type relaxation in this work.

We proposed to use a diagonal preconditioner as presented in [22]. The idea is to compute the diagonal values of system matrix at each node, *e.g.* the preconditioner to solve equation (23) at node i reads:

$$M_i^d = \sum_{e} \sum_{g=1}^{8} \sum_{i=1}^{8} \left[\left(2\mathcal{H} + \frac{g_c}{\ell_c} \right) \phi_i \phi_i + g_c \ell_c \nabla \phi_i \nabla \phi_i \right] \tag{26}$$

With this technique, one does not use any matrix, which is the so-called matrix-free type finite element methods.

The generic PCG solver is presented in the following flow chart:

- Initial guess $\tilde{\boldsymbol{x}}$ with Dirichlet boundary conditions
- Compute preconditioner vector $\boldsymbol{M}$
- $\boldsymbol{r} = \boldsymbol{F}_R - \boldsymbol{F}_L$ with $\boldsymbol{r} = \boldsymbol{0}$ on Dirichlet boundary conditions
- $ite = 1$
- while $ite \leq$ number of relaxations
  1. $z^m_{i,j,k} = r^m_{i,j,k} / M^m_{i,j,k}$
  2. update $\boldsymbol{z}$ on ghost points.
  3. $rz_{new} = \boldsymbol{r}^T \cdot \boldsymbol{z}$
  4. $\beta = rz_{new} / rz_{old}$ with $\beta = 0$ when $ite = 1$
  5. $\boldsymbol{p} = \boldsymbol{z} + \beta \boldsymbol{p}$
  6. $\boldsymbol{w} = \boldsymbol{F}_L(\boldsymbol{p})$
  7. $pw = \boldsymbol{p}^T \cdot \boldsymbol{w}$
  8. $\alpha = rz_{new} / pw$
  9. $\boldsymbol{x} = \boldsymbol{x} + \alpha \boldsymbol{p}$
  10. $\boldsymbol{r} = \boldsymbol{r} - \alpha \boldsymbol{w}$
  11. $\boldsymbol{r} = \boldsymbol{0}$ on Dirichlet boundary conditions
  12. $rz_{old} = rz_{new}$
  13. $ite = ite + 1$
- end

$\boldsymbol{x}$ represents $\boldsymbol{u}$ for mechanical equations and d for phase field equations. (i, j, k) indicates the node ID. $m = 1, 2, 3$ for the mechanical part and $m = 1$ for the phase field equation. $\boldsymbol{r}$ represents the residual which is the difference of the right and the left hand side. $\boldsymbol{p}$, $\boldsymbol{w}$ and $\boldsymbol{z}$ are temporary vectors. α and β are temporary coefficients required for the PCG method. The ghost points mentioned at the second step of the loop, are created to ensure the presence of neighbors in order to perform the integration over the entire support of the nodes of a given MPI domain. They are indispensable to apply the matrix free type FEM, after the MPI domain decomposition.

3.3 Multigrid methods

Besides the PCG solvers, intergrid operators are required in multigrid algorithms. Different from the intergrid operators presented in [21] and [22], specific treatment is required to perform phase field modeling.

Equation (18) indicates that, $\mathcal{H}$, ℓ_c and g_c on the coarse grid are required to perform multigrid methods. In this work, ℓ_c is considered as a constant, which has the same value on all grids. For g_c, which is assigned to elementary nodes, homogenization techniques are used to obtain coarse grid values as presented in [21]. Besides ℓ_c and g_c on coarse grids, $\mathcal{H}$ is also required on coarse grids. As illustrated in equation (19), $\mathcal{H}$ is computed at each Gauss integration point. Furthermore, $\mathcal{H}$ is a history variable that is to be stored over time steps. However, storing $\mathcal{H}$ at each Gauss integration point is too expensive. *e.g.*, for N^3 8-node cubic elements, it is 8 times more expensive to store $\mathcal{H}$ at the Gauss integration point than storing a single representative value for each element. To save memory space, we thus propose to store $\mathcal{H}$ at each element. It

is obtained by a simple average of 8 values at Gauss integration points in each element. The integration of the initial phase field problem is thus approximated but, it will be demonstrated in the examples presented in the last Section that it does not introduce any bias in the overall problem resolution. For the $\mathcal{H}$ on coarse grids, we proposed to generate them by a simple average of the corresponding elements from the finest grid. It can be computed recursively as presented in [21].

With $\mathcal{H}$, ℓ_c and g_c on coarse grids, the PCG relaxations can be executed without any obstacles for equation (18). To transform the correction and the residual between grids, standard trilinear prolongation and restriction operators are used.

To solve equation (14), equations (12) and (13) have to be updated at each time step, due to the change of d.

As mentioned above, one uses the strategy of one voxel per elementary node. Initial material properties are therefore assigned to each node. However, in finite element methods, what we use is the material property at the Gauss integration points. One proposes to perform an interpolation with the above mentioned shape function. For example for the shear modulus, it reads:

$$G^g = \sum_{i=1}^{8} \phi_i G_i \tag{27}$$

where G^g denotes the shear modulus at a Gauss integration point and G_i is the nodal shear modulus. i is the node id. However, when we apply it to equation (13), it becomes a little more complicated due to the presence of d. The d at Gauss integration points must firstly be computed:

$$\begin{cases} d^g = \sum_{i=1}^{8} \phi_i d_i & \Phi^+ \geq \Phi^- \\ d^g = 0 & \Phi^+ < \Phi^- \end{cases} \tag{28}$$

where d^g denotes d at Gauss integration points. d_i is the nodal value. G is then computed at Gauss integration points by equation (27). Finally, G_d at Gauss integration points, reads:

$$G_d^g = [(1-k)(1-d^g)^2 + k] \cdot G^g \tag{29}$$

Applying the above strategy on the finest grid is straightforward and mandatory. However, to obtain K_d and G_d on coarse grids requires several specific treatments.

As demonstrated in equations (12) and (28), one must first compute $tr(\boldsymbol{\epsilon})$, Φ^+ and Φ^- to define K_d and G_d at each Gauss integration point. To compute $tr(\boldsymbol{\epsilon})$, Φ^+ and Φ^-, the displacement $\boldsymbol{u}$ is indispensable. However, in phase field modeling, the structure is globally under traction or shearing, *i.e.* $tr(\boldsymbol{\epsilon}) \geq 0$. Nevertheless, compression, *i.e.* $tr(\boldsymbol{\epsilon}) < 0$, can be presented in several small zones, or even several nodes on the finest grid. But, on coarse grids, the displacement has been homogenized, one may not find compression on the coarse girds. Using the displacement on coarse grids to obtain $tr(\boldsymbol{\epsilon})$, Φ^+ and Φ^-, can therefore not guarantee a reasonable representation of the original problem on coarse grids. It can cause slow convergence and even divergence in multigrid algorithms. By consequence, we propose to compute these criteria on Gauss integration points at the finest girds. For the K_d and G_d on coarse grids, the following strategy is proposed:

- Calculate the value of K, G and d at Gauss integration points on the finest grid.
- Compute $tr(\boldsymbol{\epsilon})$, Φ^+ and Φ^- at these Gauss integration points on the finest grid.
- Obtain K_d and G_d at these Gauss integration points on the finest grid.
- Calculate the average of K_d and G_d of all Gauss points in each element. These averages, *i.e.* K_e and G_e, represent elementary material property on the finest grid.

- Compute K_e and G_e in each element on coarse girds with homogenization techniques presented in [22].

The idea of the above strategy is to use the averaged K_d and G_d to transfer Gauss integration point material property to element. The coarse gird material property is then computed directly from K_e and G_e on the finest grid. The best representation of the original problem is achieved. Note that our objective is to solve the problem on the finest grid, the existence of coarse grids is to improve convergence rate. That is why on coarse grid, we do not seek an exact solution of the original problem but making several modifications to achieve the best convergence.

The prolongation and restriction operators used for solving equation (14) are tri-linear standard operators.

For details of the multigrid algorithm, please refer to our previous work [21, 22]. Here, we just take some notations. The full multigrid (FMG) cycle and V-Cycle are used in this work. Figure 2 presents a 3-level FMG scheme. One performs ν_0 relaxations on level 1, ν_1 relaxations on each level going up and ν_2 relaxations on each level going down. n_{cy} V–Cycles are used on each level. A trilinear interpolation of the solution of level l is applied to obtain the initial solution of level $l+1$. The V–Cycle program for the PCGMG method is illustrated in the

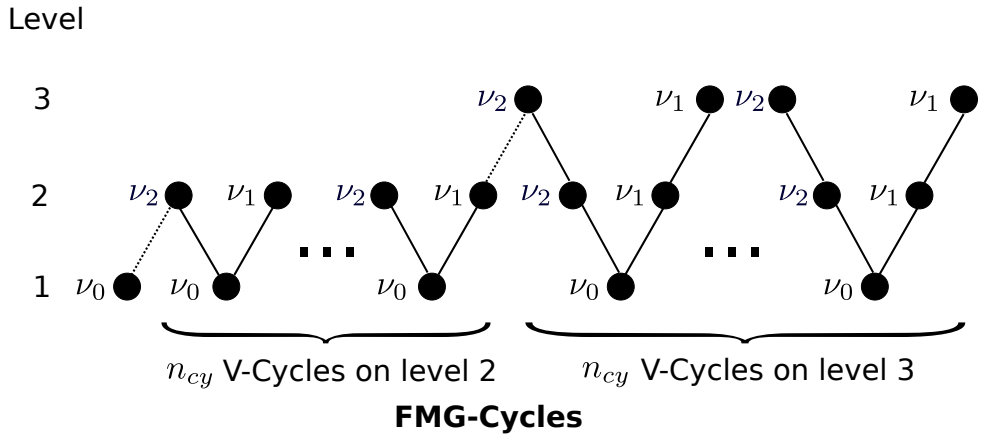

Figure 2: FMG cycles

following flow chart:

1. Compute the coarse grid material property.
2. Carry out ν_2 relaxations with the PCG solver on the finest level l.
3. Inject the solution and restrict the residual to level $l-1$.
4. Perform ν_2 relaxations on level $l-1$.
5. Repeat steps 3,4 until the coarsest grid $l=1$.
6. Perform ν_0 relaxations on level 1.
7. Prolong the correction to the next finer level and perform ν_1 relaxations on this level.
8. Repeat step 7 until the finest level.
9. Loop step $2-7$ until obtaining the required relative error.
10. Output results

3.4 Overall program

The above sections introduce each part of the phase field modeling. In this section, the entire program to perform the phase field modeling in heterogeneous materials is presented.

Besides of the numerical efficiency, the hybrid MPI/OpenMP is also applied to achieve the best performance both on memory and computational time. The entire program is described in the following flow chart.

- Create MPI topology
- Input images and obtain g_c, K and G on the finest grid.
- Calculate g_c on all coarse grids
- $t = 0$ and initialization of vectors
- while $t \leq$ number of time step
  1. if (t=0)
     (a) Compute material properties, *i.e.* K_e and G_e, depend on d on all grids
     (b) Compute U_e where $max(W(\boldsymbol{x})) = \Phi_c$
     (c) $U_t = U_e$
  2. else
     (a) Calculate prescribed displacement $U_t = U_t + \delta U$
     (b) Compute material properties depend on d on all grids
     (c) Compute $\boldsymbol{u}_t$ always with a prescribed displacement U_{unit} but a new d
     (d) Compute $\mathcal{H}$ with $\frac{U_t}{U_{unit}}\boldsymbol{u}_t$
     (e) Compute the right hand of equation (18)
     (f) Compute d with the new $\mathcal{H}$
     (g) output d
  3. end if
- end

From the above algorithm, we can find that, in step 2.(c), instead of computing the displacement with the updated d and U_e, we propose to always compute the solution $\boldsymbol{u}_t$ with the same boundary condition U_{unit} and an updated d. Because equation (14) is a static linear elastic problem at each time step, its solution $\boldsymbol{u}_t$ is proportional to the prescribed displacement. With this strategy, one can minimize changes in the displacement solution on going to the next time step. It can lead to a faster convergence speed when using an iterative solver.

4 Performance analysis

In this section, the convergence performance of the proposed method is analyzed. Some improvements are also investigated. The parallel performance is also demonstrated at the end of this section.

4.1 Convergence performance of the proposed algorithm

The performance of the PCGMG method is firstly analyzed by solving a spherical inclusion problem in a linear elastic domain Ω as illustrated in Figure 3. The cube size is L. Ω is

discretized by 128^3 elements. A 6-level multigrid algorithm is applied. The element size on level l is 2 times larger along each direction than on level $l+1$. For this first example, we propose to use simple trilinear restriction and prolongation operators to ensure the transfers between grids. The material properties on coarse grids are computed by a simple average of the material property at corresponding nodes (or element, depending on parameters) from the finest grid. The matrix and the inclusion have the same Poisson ratio $\nu = 0.29$. The Young's modulus of the matrix is $E_M = 233.43$ GPa. Supposing the Young's modulus of inclusion E_I is smaller than E_M, the contrast is defined by:

$$c = \frac{E_M}{E_I}$$

The following boundary conditions are prescribed:

$$\begin{cases} u_z = U_o & \text{on } z = L. \\ u_z = 0 & \text{on } z = 0. \\ u_x = 0 & \text{at node } (\frac{L}{2}, 0, 0) \\ u_y = 0 & \text{at node } (0, \frac{L}{2}, 0) \end{cases}$$

To analyze the convergence performance, the relative residual Rr is computed by the following

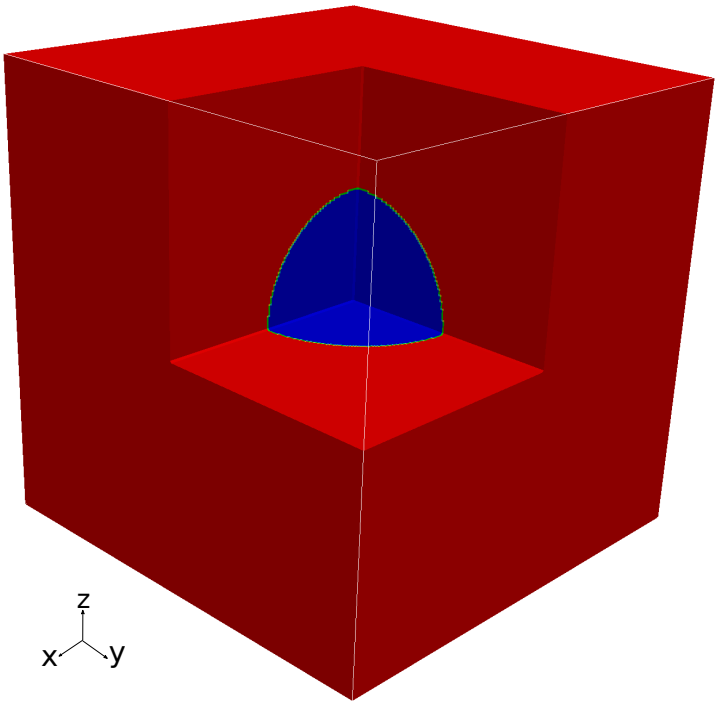

Figure 3: Spherical inclusion in a linear elastic domain

equation:

$$Rr = \frac{r^T \cdot r}{F_R^T \cdot F_R} \times 100\% \tag{30}$$

Figure 4 illustrates the convergence performance for the single level PCG solver and the PCGMG method with a material contrast $c = 1000$. The relative residual to be reached is set to be: $Rr \leq 10^{-6}$. A 2-1 V-Cycle is used for the PCGMG solver, which means $\nu_2 = 2$ and $\nu_1 = 1$. Supposing the cost of the transform between grids is negligible, the total cost of a 5 V-Cycle PCGMG is equivalent to 17 relaxations on the finest grid. On the other hand, to achieve the required Rr, the single level solver takes 445 relaxations, which is 26 times more expensive than the PCGMG solver.

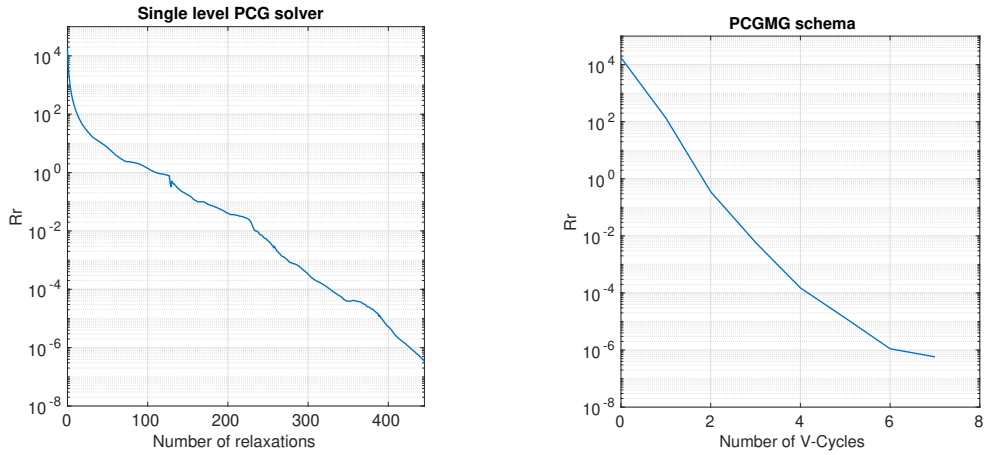

(a) Single level PCG algorithm (b) PCGMG algorithm

Figure 4: Convergence of single level PCG and PCGMG algorithms

Figure 5 presents the convergence performance of the Jacobi solver based multigrid and PCG based multigrid for different material property contrasts. From this Figure, we can conclude: (1), A large contrast, *e.g.* $c = 1000$ can lead to non-convergence with the Jacobi based multigrid method. (2), PCGMG is more efficient (faster convergence) than Jacobi based multigrid even for small contrast cases, *e.g.* $c = 10$. (3), PCGMG is robust even when the contrast is closed to the numerical precision, *e.g.* $c = 10^{12}$.

To analyze the locking effect in multigrid methods, the Poisson ratio ν is set to be 0.49 with $c = 1000$. Figure 6 illustrates the evolution of the relative residual Rr of PCGMG algorithms. The convergence speed is less than the problem with $\nu = 0.29$, but it converges. With the Jacobi based multigrid algorithms, we obtain a divergence from the first relaxation onward.

According to the performance analysis carried out on the spherical inclusion problem, we confirmed that: (1), PCGMG can handle problems with large material property variations which is the case in phase field models; (2), PCGMG is able to overcome the locking effects; (3), PCGMG is much more efficient than the Jacobi solver based multigrid algorithm; (4), The strategy to use a PCGMG algorithm is much more efficient than a single level PCG solver.

However, as presented in [21] and [22], the spherical inclusion is a simple problem with a regular and symmetric geometry. The real microstructure of heterogeneous materials is much more complicated than a spherical inclusion. A standard multigrid method may not be so efficient for handling complex microstructures. A homogenization technique was therefore proposed in [21] and [22] to compute material properties on coarse grids. It can guarantee a reasonable representation of the finest grid problem on coarse grids. Here, we use the real tomographic image of nodular graphite cast iron to analyze the convergence performance of such a proposed homogenization technique for solving a problem with a stress singularity.

As presented in Figure 7, a region of interest with 257^3 voxels is taken from the image of graphite cast iron obtained by [2]. The voxel size is 5.06 μm. The strategy to obtain the material property from the gray level in the image is presented in [22]. The material property of each material illustrated in Table 1 is applied. The convergence performance is analyzed with an initial crack.

In this work, we propose to work in voxel. The size of the entire domain Ω is 256^3 voxels. 256^3 8-node cubic elements are used to discretize Ω. The initial crack is prescribed as:

$$d = 1 \text{ when } x < 25.6 \,\&\, z = 127, 128, 129$$

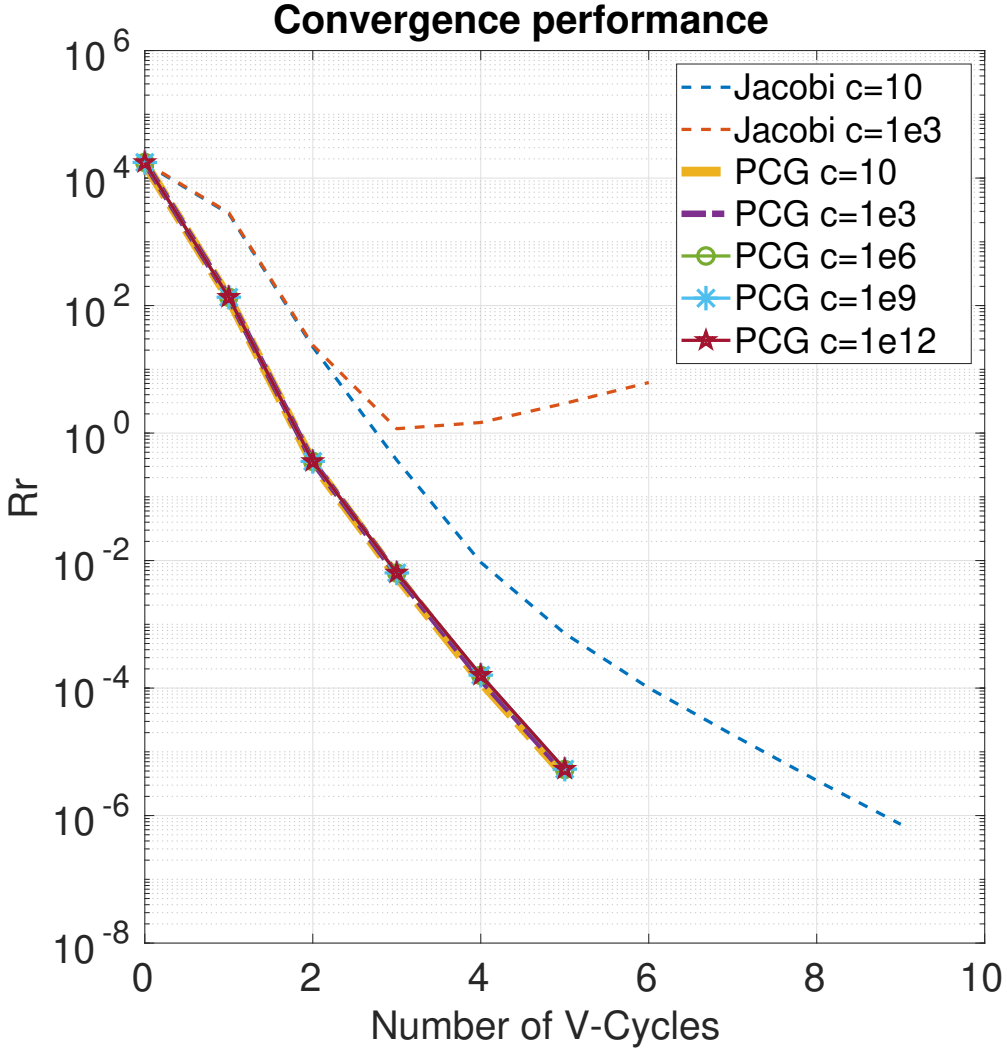

Figure 5: Convergence performance of Jacobi based multigrid and PCG based multigrid for different material property contrasts

Table 1: Material properties in cast iron

Material	E/GPa	ν	g_c/kN·mm^{-1}
Iron	210	0.2	1.73×10^{-3}
Graphite nodules	21	0.3	1.8×10^{-4}

which is illustrated in Figure 8. The following boundary conditions are applied :

$$\begin{cases} u_z = 1 & \text{on } z = 256 \\ u_z = 0 & \text{on } z = 0 \\ u_x = 0 & \text{at node } (128, 0, 0) \\ u_y = 0 & \text{at node } (0, 128, 0) \end{cases}$$

The small parameter k is set to 10^{-5}, $\ell_c = 2h$ with element size h. A 7-level multigrid algorithm is applied. The element size on level l is 2 times larger than on level $l+1$. V-Cycles with $\nu_2 = 2$ and $\nu_1 = 1$ are used to solve equation (18). However, $\nu_2 = 4$ and $\nu_1 = 2$ are applied for

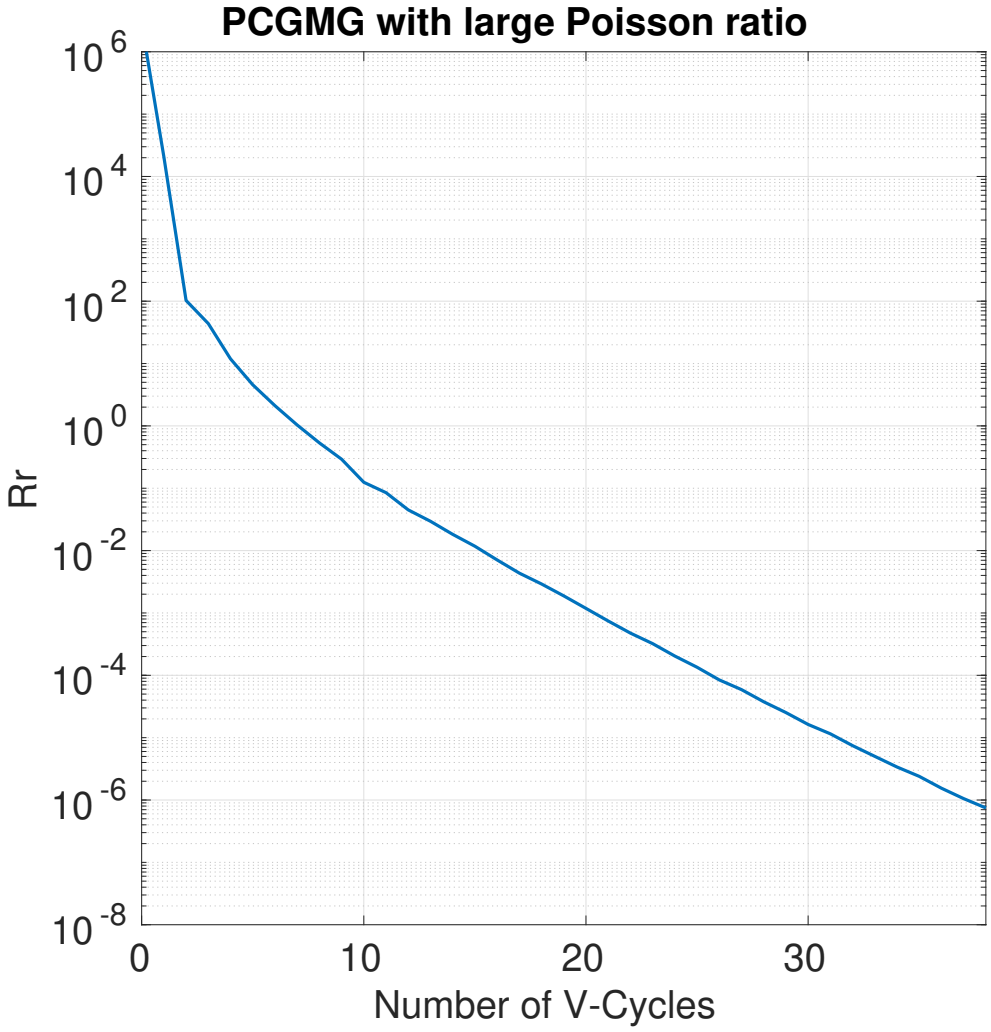

Figure 6: Convergence performance of PCGMG solver with $\nu = 0.49$

solving equation (14) due to higher complexity. A trilinear restriction and prolongation operator is used for solving both equations. A problem is supposed to be converged when $Rr \leq 10^{-6}$. The problem is solved by using different strategies for estimating material properties on coarse grids. A first simulation is performed in which material properties on coarse grids are obtained by averaging material properties at corresponding nodes from the finest grid. An other strategy is to use the advanced technique proposed in [21] and [22] to recursively compute material properties on coarse grids.

Figure 9a shows that the advanced technique may not give a significant improvement when solving equation (18). Because the best performance is already achieved with a simple average. But for equation (14), as presented in Figure 9b, the advanced technique can distinctly improve the convergence performance, *i.e.* the simulation is 2 times cheaper. That is because a simple average of material properties on coarse grid can not guarantee a reasonable representation of the original problem for such a complex case. The result is confirmed with the proposal in [22].

4.2 Parallel performance analysis

A hybrid MPI/OpenMP code is built based on our previous work [21] and [22]. The detailed performance analysis is already presented in [21]for thermal problems. To be rigorous, a brief

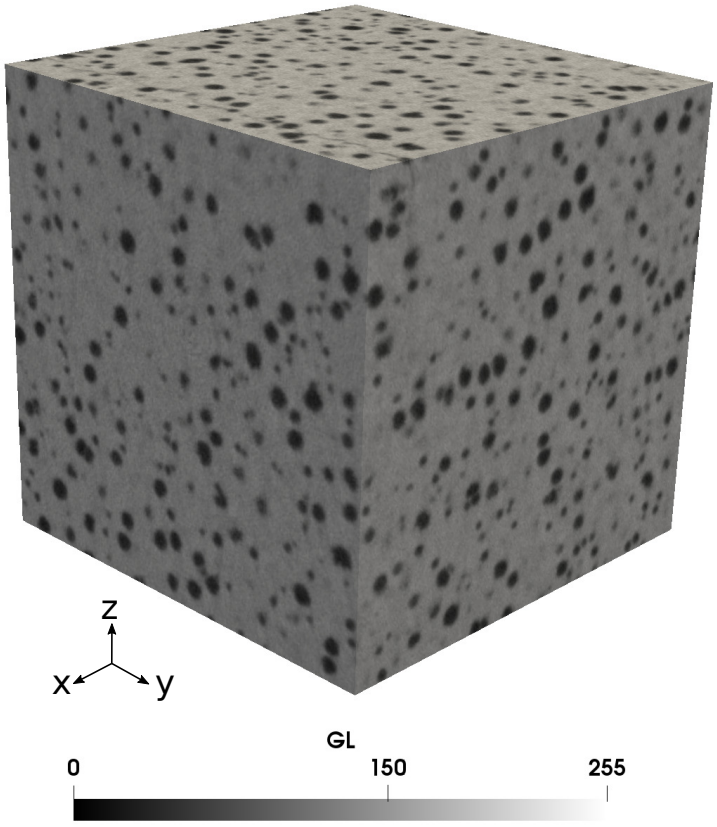

Figure 7: The gray level (GL) in image of cast iron

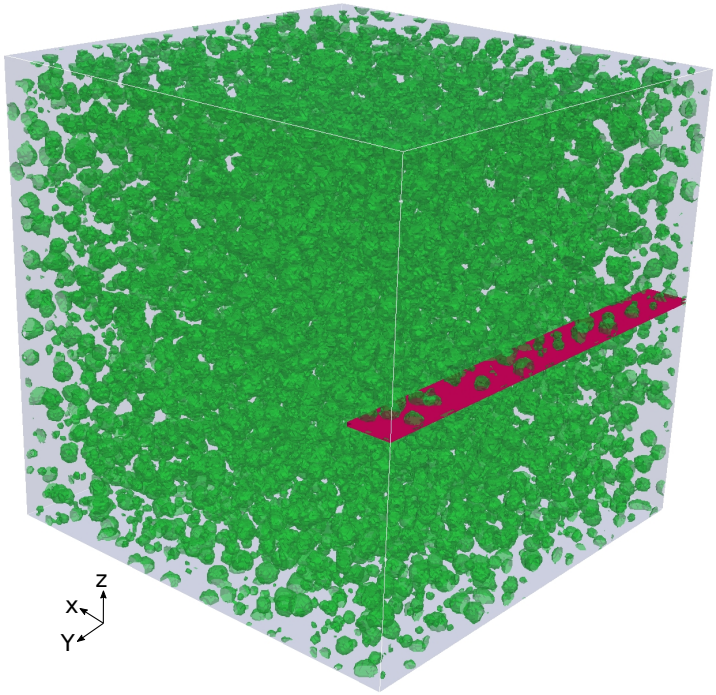

Figure 8: The prescribed initial crack. The initial crack is red and graphite nodules are green

parallel performance analysis is proposed herein. Since the analysis of the entire phase field simulation until failure is too expensive, we propose to analyze it on the previous nodular

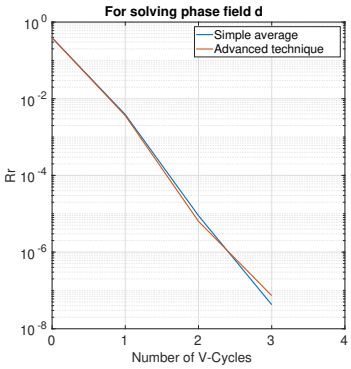

(a) For solving Equation (18)

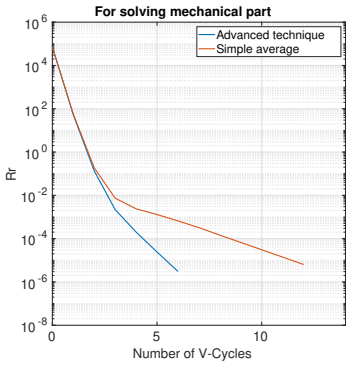

(b) For solving Equation (14)

Figure 9: Convergence performance of PCGMG algorithms with different material properties on coarse grids for both phase field problem and balance of momentum problem

graphite cast iron problem with a stress singularity. This problem with a stress singularity can be considered as a time step of phase field modeling: one resolution of the phase field problem plus one resolution of the mechanical problem. The computations are performed on the supercomputer Liger of ICI at Ecole Centrale de Nantes. Each processor of Liger computer consists in 12 cores where OpenMP and MPI can be used. Each node has two sockets or processors. Between nodes, MPI is inevitable. Between sockets, MPI is suggested since OpenMP suffers from poor data access patterns when using two sockets. As a consequence of this computer architecture, the number of OpenMP per MPI task is limited to 12. On Liger computer, each node has 128 GB memory space. With the help of the matrix free strategy, 128 GB is enough for solving on one single core the largest numerical example, *i.e.* 256^3 elements, presented in this work.

To analyze the parallel performance, the wall time is obtained with different configurations (see in Table 2) for the same simulation. Figure 10 shows the speedup as a function of the number (NB) of cores used on this 256^3 elements problem. Within 100 cores, the speedup is almost optimal. When using 384 cores, an efficiency of about 90% can be found, which means the wall time is reduced to 150 s instead of 51567 s with one core. This efficiency confirms to the result obtained in [21].

Table 2: Hybrid setting

NB of MPI	NB of OpenMP	Cores used	Nodes used
1	1	1	1
8	3	24	1
16	3	48	2
64	1	64	4
32	3	96	4
32	6	192	8
64	6	384	16

In this work, we do not show the efficiency with 1000 cores. This is because the largest numerical example presented in this work has only 256^3 elements. 384 cores are enough to solve such problem. Using more cores can slow down the speedup. Meanwhile, for an entire phase field modeling with such structure, if we have 1000 time step, it will take less than 42 hours. Note that the first time step is the most expensive one. However, if we do not use parallel

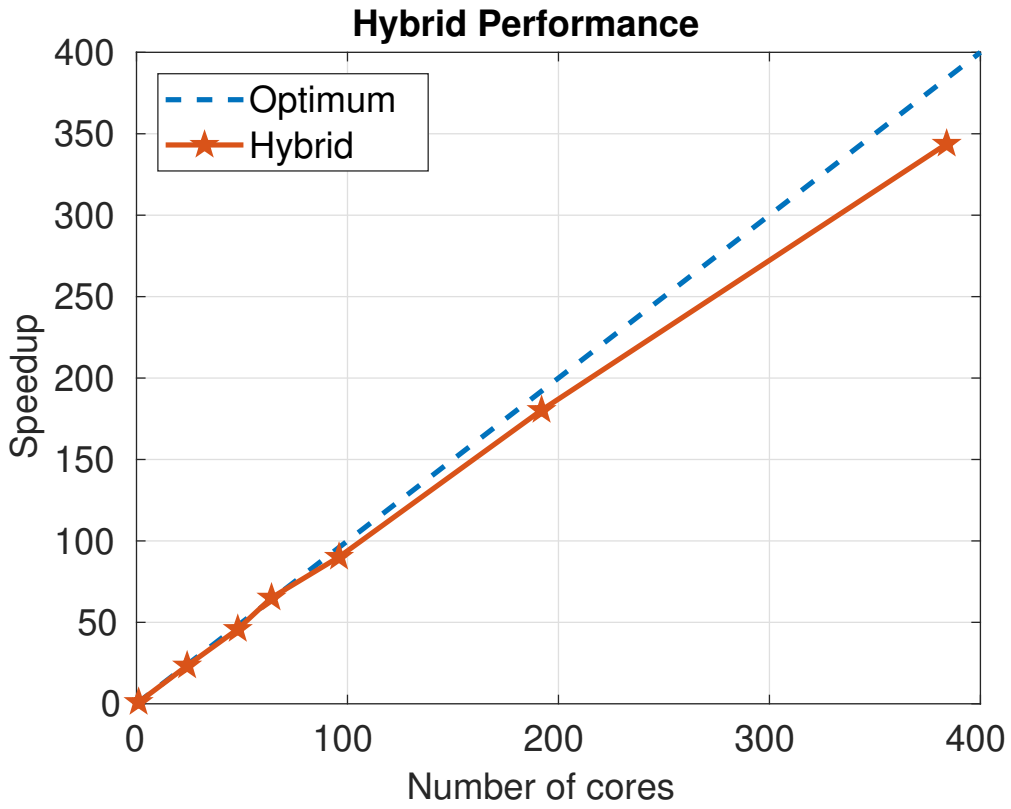

Figure 10: The parallel performance of the hybrid MPI/OpenMP strategy

computing, the computational time will be 596 days (almost two years).

5 Validation and applications

In this section, the validation of the proposed strategy is presented. Two applications are then presented to show the ability of the proposed strategy.

5.1 Validation with three dimensional single notched plate

To validate the proposed strategy, a typical crack propagation in a squared shape part with homogeneous material under a tensile loading is illustrated. The three-dimensional mode-I tension test has already been presented in [16] and [10]. However, only the crack pattern can be found in these two papers, the 3D load–displacement curve is not illustrated, which does not allow us to perform a quantitative comparison. In this work, we therefore take the 2D example parameters from the literature ([16, 10, 15]) and try to find an agreement between the 2D and 3D examples.

The dimension of the part and the initial crack are presented in Figure 11. The Young's modulus is set to be 210 GPa. Its Poisson ratio equals to 0.3. The fracture toughness g_c is set to 2.7×10^{-3} kN·mm^{-1}. The domain is discretized by $256\times64\times256$ elements. The element size is about $h = 0.0039$ mm. ℓ_c is supposed to be 0.0078 mm, which is twice the element size. The small parameter k equals to 10^{-5}. 7 levels are used for the multigrid algorithm. The element size of level $l+1$ is two times smaller than on level l. 192 cores are used to perform this simulation.

The following boundary conditions are applied:

$$\begin{cases} \boldsymbol{u} = \mathbf{0} & \text{on } z = 0 \text{ mm} \\ \boldsymbol{u} = \{0, 0, Ut\} & \text{on } z = 1 \text{ mm} \end{cases}$$

As mentioned above, the displacement is always computed with the same prescribed displacement U_{unit} but a new d. This U_{unit} equals to 1 mm in this example. The following increment is applied for this case:

$$\begin{cases} \delta U = 1e^{-5} & Ut \leq 5e^{-3} \text{ mm} \\ \delta U = 1e^{-6} & Ut > 5e^{-3} \text{ mm} \end{cases}$$

At each time step, the solution is supposed to be converged when the relative residual $Rr \leq 10^{-6}$. The same material parameters are used according to the 2D single edge notched tensile test presented in [16, 10, 15]. From the above time step displacement increment, we can find that in this example, the threshold for $\mathcal{H}$ is not applied, *i.e.* $\Phi_c = 0$, for comparing with the results from literature.

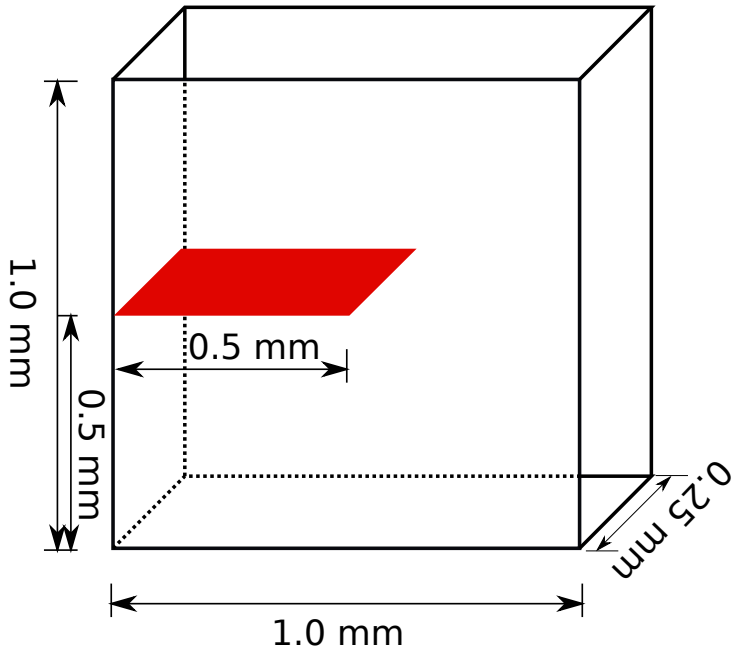

Figure 11: Geometry and initial crack

Figure 12 illustrates the crack pattern at different loading step. It confirms to the 3D results presented in [16] and [10]. From this Figure, we find that the computed crack thickness is smaller than the thickness prescribed to the initial crack. This is because $d = 1$ are prescribed on three layers of nodes to introduce the initial crack in the model. But l is set to $2h$, the computed crack thickness is therefore smaller.

To perform a quantitative 2D–3D comparison, we propose to compute the reaction force F per unit width along the Z direction. It means to divide the reaction force by the width of the domain, *i.e.* 0.25 mm. The load–displacement curve should then be similar to 2D regardless of 3D effects. Figure 13 illustrates the reaction force F on a unit width along Z direction as a function of the prescribed displacement Ut. A maximum reaction force F_{max} of 0.66 kN/mm can be found in this case. The result is similar to the 2D load–displacement curve presented in [16, 10] and [15].

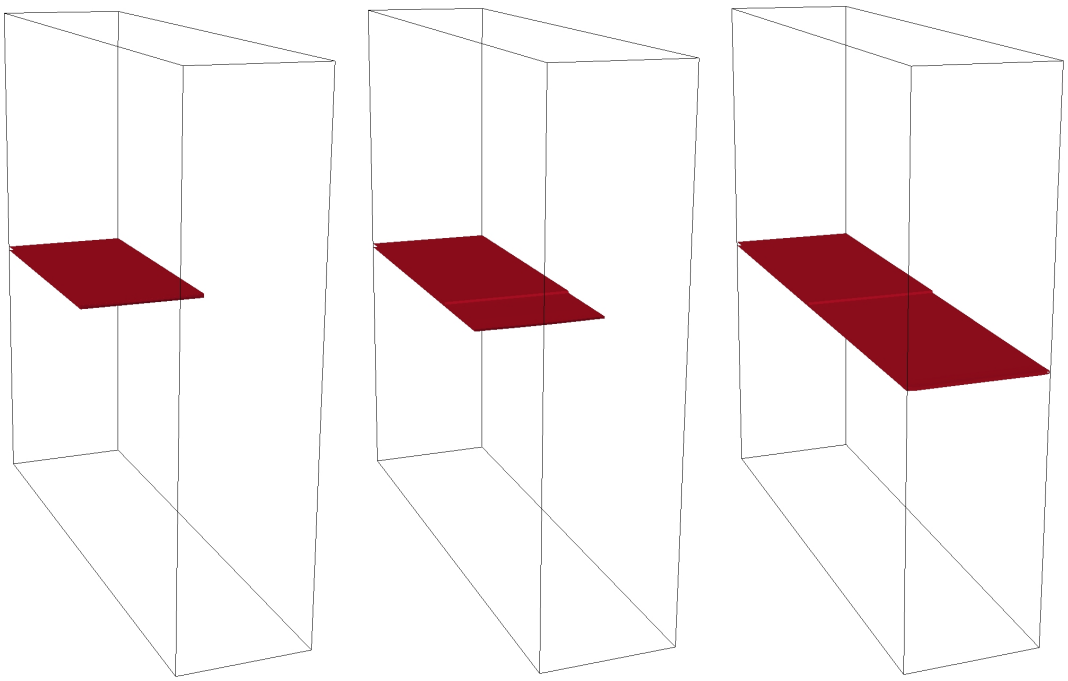

Figure 12: Evolution of crack pattern at different loading step: The isosurface of phase field d with a value of 0.99. The left crack pattern is obtained at $Ut = 0.005591$ mm, the middle one is obtained at Ut=0.006 mm, the right one is obtained at Ut=0.006273 mm.

5.2 Crack initiation and propagation in the structure with a spherical inclusion

In this section, the proposed strategy is applied for the modeling of crack initiation and propagation in a structure with a spherical inclusion as presented in Figure 3. The size of the cube-shaped structure is $128 \times 128 \times 128$ mm^3. Properties of each material are given in Table 3. One supposes that the crack resides only in the matrix. The g_c in the inclusion is therefore supposed to be 100 times greater than in the matrix. 126^3 8-node cubic elements are used to discretize the cube with the element size $h = 1$ mm. The Multigrid method uses 6 levels. At time step $t = 0$, FMG cycles are performed. However, V–cycles with $\nu_2 = 2$ and $\nu_1 = 1$ are applied for the other time steps. It is because from one time step to the next time step, the solution should not change a lot. A good initial solution is already obtained. V–Cycles are therefore the best choice. $\ell_c = 2h$ is applied. 192 cores are used to perform this simulation. The following boundary conditions are prescribed:

$$\begin{cases} u_z = U_t & \text{on } z = 128 \text{ mm} \\ u_z = 0 & \text{on } z = 0. \\ u_x = 0 & \text{at node } (64, 0, 0) \text{ mm} \\ u_y = 0 & \text{at node } (0, 64, 0) \text{ mm} \end{cases}$$

At each time step, the solution is supposed to be converged when the relative residual $Rr \leq 10^{-6}$. At $t = 0$, $U_e = 0.138$ mm is obtained.

For the displacement increment δU, in this work, we propose an automatic load control strategy to better manage the crack propagation. As is well-known, the basic hypothesis of the staggered phase field is that: the solution increment shall be sufficiently small and the system shall be stable to guarantee a good approximation of the monolithic problem. It means that d should not change a lot from one time step to the next one. We therefore propose to compute

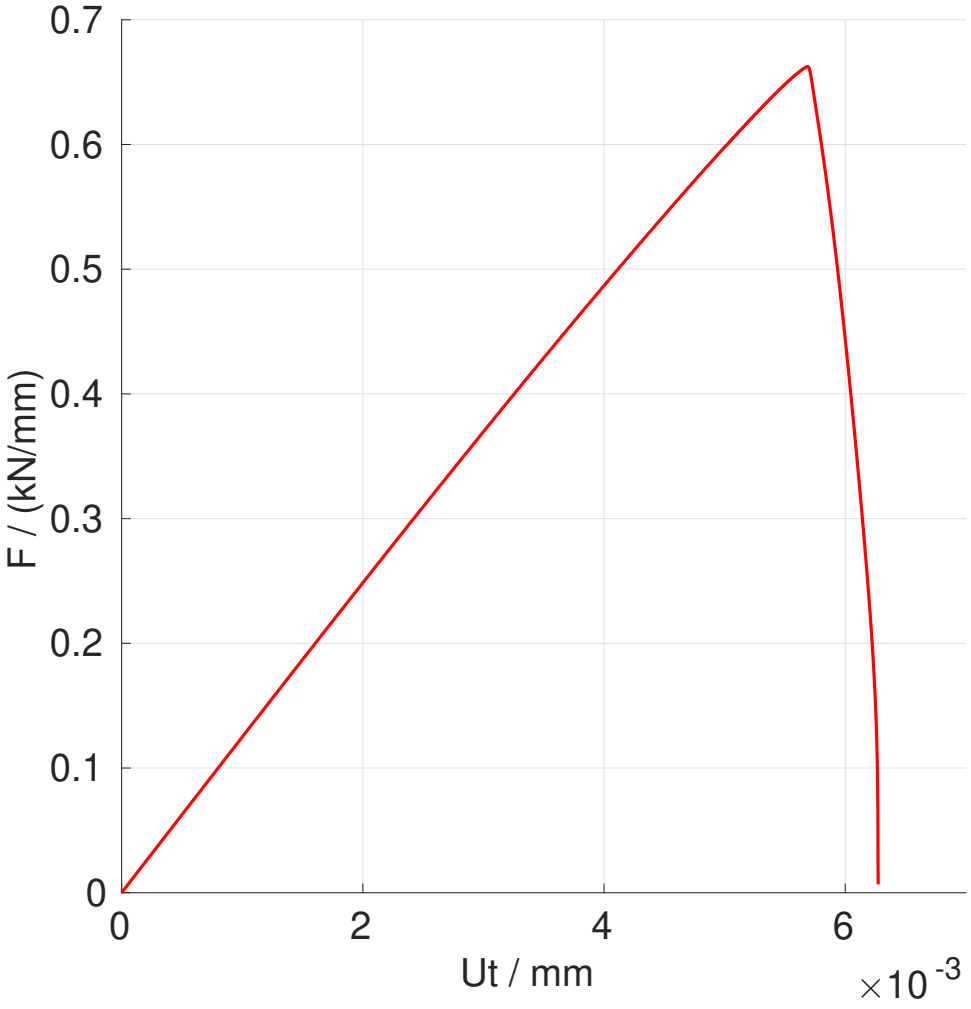

Figure 13: Reaction force in function of prescribed displacement

Table 3: Material properties in spherical inclusion problem

Component	E/GPa	ν	g_c/kN·mm^{-1}
Matrix	233.43	0.29	2.7×10^{-3}
Inclusion	2334.3	0.29	2.7×10^{-1}

the maximum value of the variation of d from time step t to the time step $t+1$ over the entire domain. It reads:

$$\delta d_{max} = max(d_i^{t+1} - d_i^t)$$

where d_i^t and d_i^{t+1} are the nodal values of d over the entire domain at time step t and $t+1$, respectively. δd_{max} thus estimates the maximum value of the variation of d over the entire domain. The automatic time step control system is constructed based on δd_{max}. The principle is to increase δU when δd_{max} is too small, and to reduce δU when δd_{max} is too large.

For this spherical inclusion problem, the following guidelines are proposed as a first attempt:

$$\delta U^{t+1} = \begin{cases} 2\delta U^t & \delta d_{max} \leq 0.01 \\ \delta U^t & 0.01 < \delta d_{max} < 0.1 \\ 0.5\delta U^t & \delta d_{max} \geq 0.1 \\ 0.01Ue & \delta U^t \geq 0.01Ue \end{cases}$$

where δU^t denotes the value of δU at time step t, with $\delta U^1 = 0.01Ue$ at t=1. To avoid a too large displacement increment, the maximum value of δU is limited at $0.01Ue$.

A fully cracked structure as presented in Figure 14b is obtained at time step $t = 91$. The top fracture pattern confirms the result presented in [16]. Only one crack pattern can be found in [16], that is because they used irregular meshes and a refinement only on the top. It is well-known that strain concentration can be found on the two poles of the sphere. Multicrack is expected with this symmetric structure without local defects. The Z direction external force versus the displacement response is illustrated by the red solid line in Figure 15.

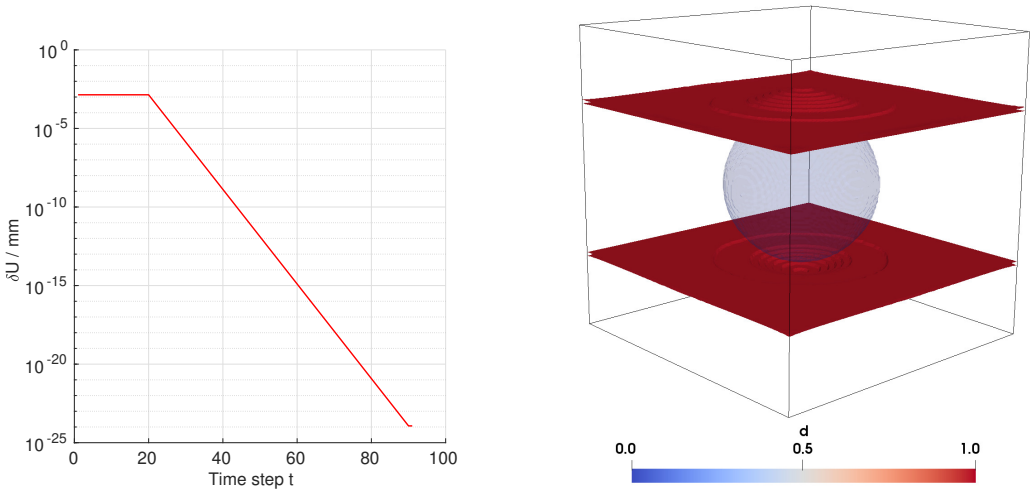

(a) δU in function of t

(b) Failure at time step $t = 91$

Figure 14: Displacement increment applied and the fully broken structure

The above result seems to be correct. However, analyzing Figure 14a, one finds that the crack continues to propagate even when δU becomes very close to 0, *i.e.* 10^{-15} mm. Meanwhile, with only 91 time steps, the crack initiation and propagation are obtained even with a such small displacement increment. It means that the crack propagation might be unstable and the crack propagates too fast.

As a consequence, the stability of the above system at each time step is suspect. The snap-back behavior during the crack propagation proposed in [33] and [34] is therefore considered. The idea is to allow a decrease fo the prescribed displacement during crack propagation, *i.e.* applying negative δU. The following automatic control strategy is then proposed. For $\delta U^t > 0$

$$\delta U^{t+1} = \begin{cases} 2\delta U^t & \delta d_{max} \leq 0.01 \\ \delta U^t & 0.01 < \delta d_{max} \leq 0.05 \\ 0.2\delta U^t & 0.05 < \delta d_{max} \leq 0.15 \\ 0.1\delta U^t & \delta d_{max} > 0.15 \\ 0.01Ue & \delta U^t \geq 0.01Ue \\ -10^{-9} & \delta U^t \leq 10^{-9} \end{cases}$$

For $\delta U^t < 0$

$$\delta U^{t+1} = \begin{cases} 0.5\delta U^t & \delta d_{max} \leq 0.01 \\ \delta U^t & 0.01 < \delta d_{max} \leq 0.05 \\ 5\delta U^t & 0.05 < \delta d_{max} \leq 0.15 \\ 10\delta U^t & \delta d_{max} > 0.15 \\ -0.01Ue & \delta U^t \leq 0.01Ue \\ 10^{-9} & \delta U^t \geq -10^{-9} \end{cases}$$

with $\delta U^1 = 0.01Ue$ at t=1.

Figure 17 illustrates the crack at different time steps with automatic load control. Here, 421 time steps are required to reach complete failure. The failure starts at the two poles of the sphere. It is consistent with zones where there are stain concentration on linear elastic problem as obtained in [22]. A significant difference can be found at the final failure between strategies with and without snap-back, especially for the top crack. Note that the non-symmetric crack patterns for the top and the bottom crack are consistent with the symmetry break introduced by the boundary conditions detailed above. The blue dashed line in Figure 15 shows a typical snap-back behavior. It is obtained that the maximum value of the external force is almost the same. It also confirms that during the macroscopically elastic part, the structure is stable. However, once exceeding this phase, the structure becomes unstable and the snap-back behavior is therefore obtained. Figure 16 presents the evolution of δd_{max} as a function of the time step t. To simplify the comparison, the two curves are plotted in the same X scale. It is obvious that without snap-back the δd_{max} remains large after crack initiation, even the load increment vanishes. However, with snap-back, only one pic in δd_{max} can be found at the end of crack propagation. To be quantitative, the average of δd_{max} over time steps is calculated for these two strategies. 0.20 is obtained for the strategy without snap-back. For the strategy with snap-back, one obtains 0.06. It confirms that the automatic load control strategy allowing snap-back can guarantee a minimum variation of d for each time step. It thus legitimates the staggered resolution strategy of the phase field problem.

5.3 Crack initiation and propagation in cast iron

In this section, the crack propagation is studied in a real image of cast iron as presented in Figure 7. The geometry and material properties were detailed in Table 1. The finite element discretization strategy and the multigrid parameter setting are the same for the cast iron example presented in Section 4. 384 cores are used to perform this simulation. Here, we work with a voxel size of 5.06 μm. Different from Section 4, here, the phase field modeling is performed without an initial crack. It allows one to analyze the crack initiation and propagation. The following boundary conditions are prescribed:

$$\begin{cases} u_z = Ut & \text{on } z = 256 \\ u_z = 0 & \text{on } z = 0 \\ u_x = 0 & \text{at node } (128, 0, 0) \\ u_y = 0 & \text{at node } (0, 128, 0) \end{cases}$$

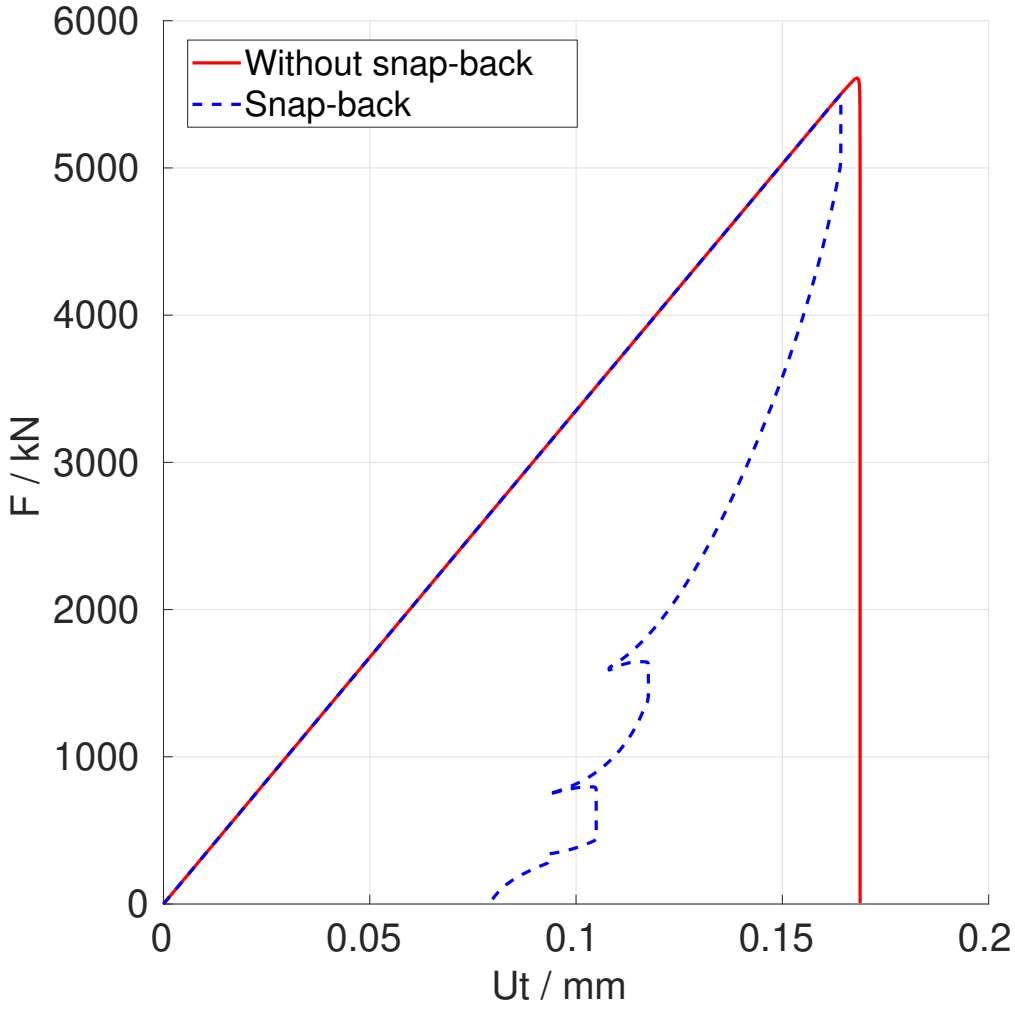

Figure 15: Snap-back behavior

The above mentioned automatic load control strategy is applied. It reads: For $\delta U^t > 0$

$$\delta U^{t+1} = \begin{cases} 10\delta U^t & \delta d_{max} < 0.0001 \\ 2\delta U^t & 0.0001 \leq \delta d_{max} < 0.01 \\ \delta U^t & 0.01 \leq \delta d_{max} \leq 0.05 \\ 0.2\delta U^t & 0.05 < \delta d_{max} \leq 0.15 \\ 0.1\delta U^t & \delta d_{max} > 0.15 \\ 0.1Ue & \delta U^t \geq 0.1Ue \\ -10^{-9} & \delta U^t \leq 10^{-9} \end{cases}$$

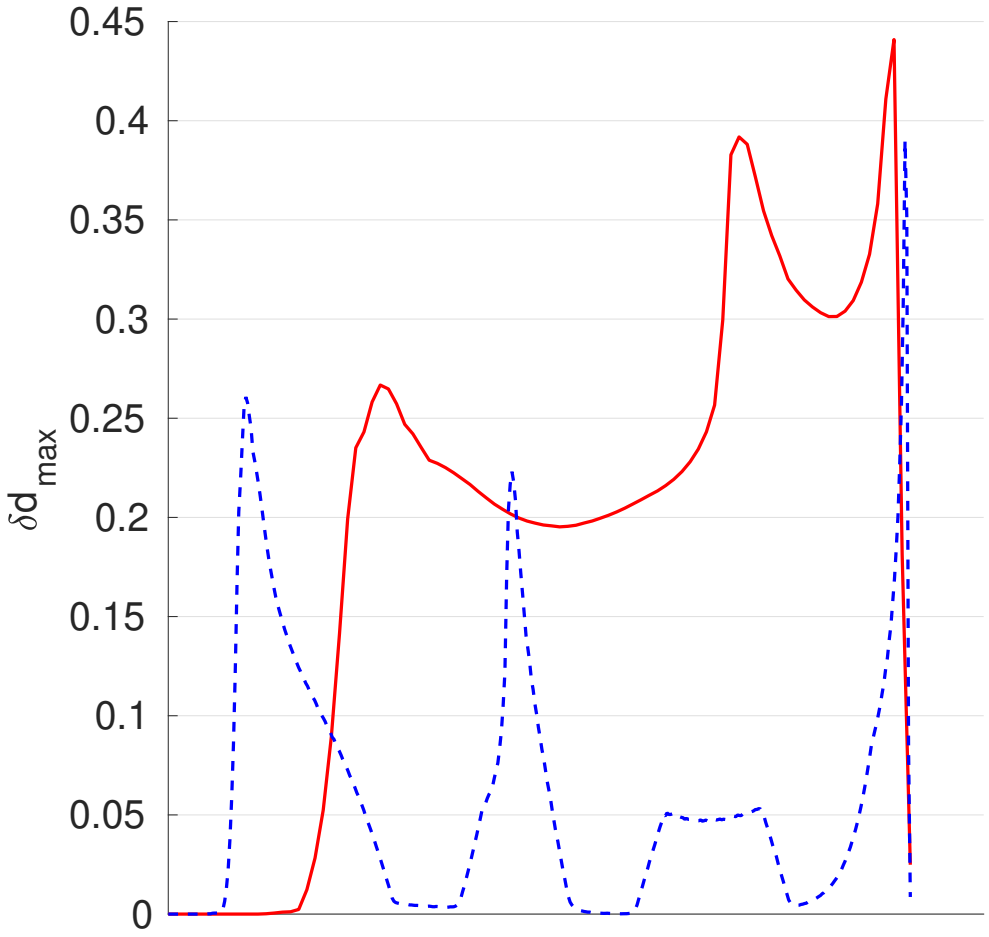

Figure 16: Comparison of δd_{max} between two displacement increment strategies

For $\delta U^t < 0$

$$\delta U^{t+1} = \begin{cases} 0.1\delta U^t & \delta d_{max} < 0.0001 \\ 0.5\delta U^t & 0.0001 \leq \delta d_{max} < 0.01 \\ \delta U^t & 0.01 \leq \delta d_{max} \leq 0.05 \\ 5\delta U^t & 0.05 < \delta d_{max} \leq 0.15 \\ 10\delta U^t & \delta d_{max} > 0.15 \\ -0.1Ue & \delta U^t \leq 0.1Ue \\ 10^{-9} & \delta U^t \geq -10^{-9} \end{cases}$$

with $\delta U^1 = 0.1Ue$ at t=1. $Ue = 0.064$ is obtained at $t = 0$. The Z direction external force as a function of the prescribed displacement is presented in Figure 18. A snap-back behavior can be found.

Figure 19 illustrates the crack in cast iron at t=100. Different from the crack propagation in homogeneous materials, the crack path is strongly affected by the graphite nodules. As obtained experimentally under cyclic loading in [2], the presence of graphite nodules also strongly affected the crack initiation and propagation. The crack surface is therefore no-longer a plane as presented in Figure 20. Meanwhile, multi-cracking can be found. It confirms the ability to

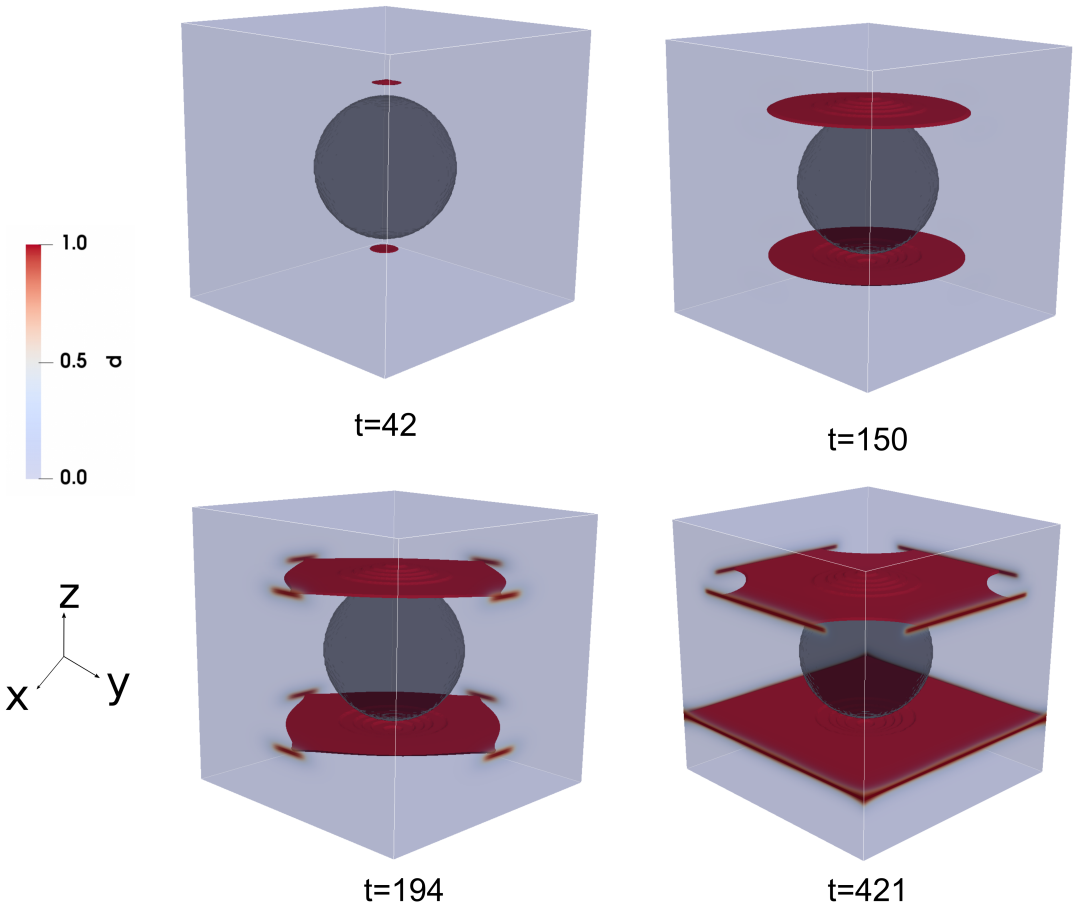

Figure 17: Crack initiation and propagation in spherical inclusion

handle multi-cracking by using the phase field modeling.

6 Conclusions and perspectives

6.1 Conclusions

In this work, a new and efficient numerical strategy is proposed to solve phase field modeling of fracture problems. The matrix–free algorithm is applied to reduce memory requirement and improve parallel performance. PCGMG algorithms permit one to handle large jumps due to the presence of crack. The automatic load control strategy allows us to observe the snap-back behavior during the crack propagation. Several complicated simulations of fracture problems in heterogeneous materials are demonstrated for the first time. The numerical results confirm several phenomena observed during experiments. The micro-macro interactions are well revealed by these complicated numerical examples. It confirms the effect of the microstructure on the macroscopic behavior. This work opens up a new path for solving large scale 3D fracture problems.

6.2 Perspectives

The automatic load control strategy proposed in this work is not perfect. It should be adapted for different problems. A more general strategy could be investigated in the future. However, the

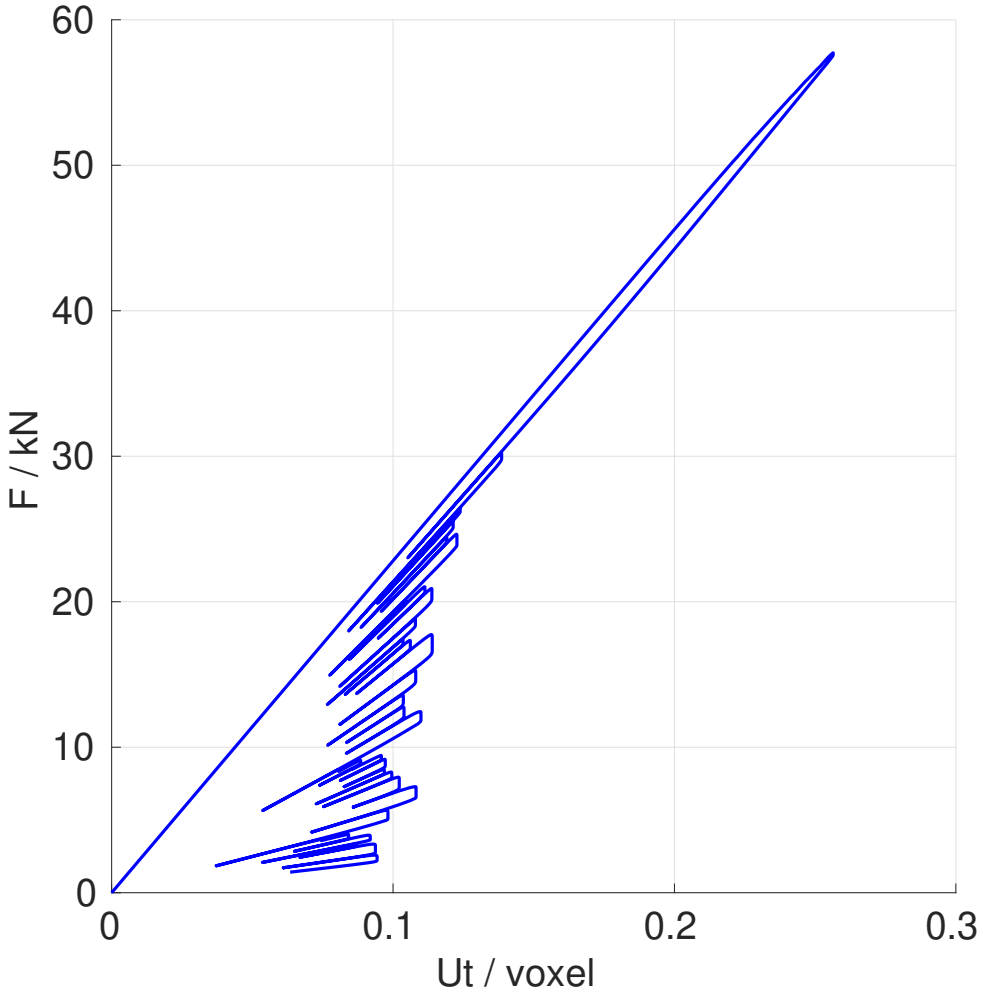

Figure 18: Load–displacement curve in cast iron until time step $t = 2390$

proposed strategy ensures that the local dissipation does not exceed a given threshold related to the maximum value of the rate of d. In the obtained load-displacement curves, it is observed that our strategy leads sometimes to unrealistic elastic unloading-reloading due to a too high decrease of the displacement increment. But, as there is no spurious energy dissipation during these artifacts, the envelop of the load-displacement curve as well as the damage evolution over time is well controlled and not biased.

Acknowledgments

The support of Région Pays de la Loire and Nantes Métropole through a grant Connect Talent IDS is gratefully acknowledged.

A A short comparison between the automatic load-control and the arc length strategy

To validate the proposed load control strategy, a short comparison is proposed using a crack nucleation problem for a one-dimensional bar with a reduced cross section under tension. The

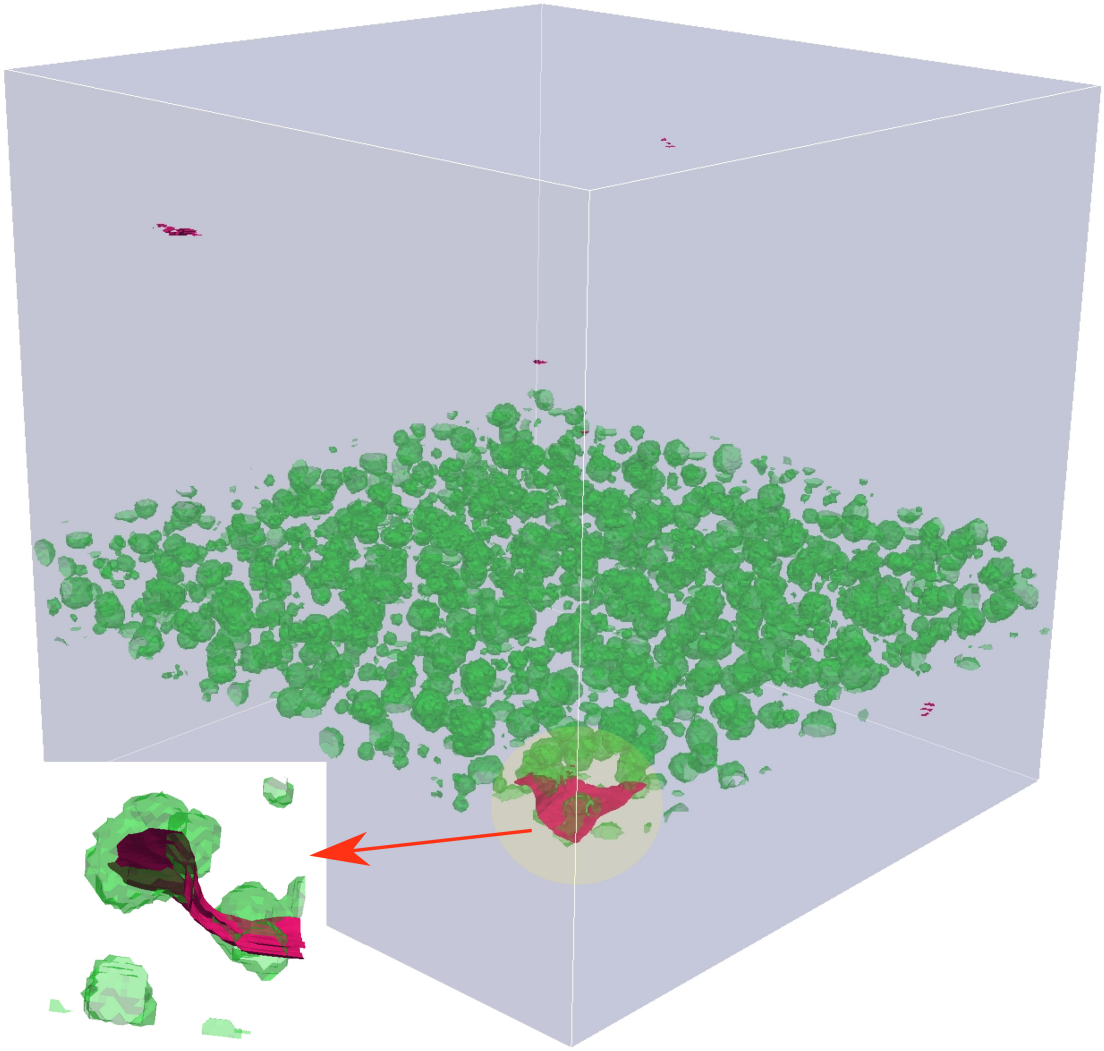

Figure 19: Crack initialization in cast iron. Graphite nodules in green and the crack in red

reference example is taken from [35]. The geometry of this 1D bar is presented in Figure 21. The same parameter is applied according to [35]. Its length L equals to 1 mm. The cross section A is set to 1 mm^2. This bar is composed of a linear-elastic material with $E = 10$ MPa and $g_c = 0.1$ N/mm. The origin of axis X is at the center of the bar. It holds therefore a domain with [-$L/2$, $L/2$]. At $x = -L/2$, the bar is fixed. A prescribed displacement Ut controlled using the proposed strategy is applied at $x = L/2$. The internal length scale ℓ_c is set to $0.05L$. The element size h equals to $\ell_c/32$.

The following automatic load control system is applied: for $\delta U^t > 0$

$$\delta U^{t+1} = \begin{cases} 2\delta U^t & \delta d_{max} < 0.001 \\ \delta U^t & 0.001 \leq \delta d_{max} \leq 0.00125 \\ 0.001\delta U^t & \delta d_{max} > 0.00125 \\ 10^{-3} & \delta U^t > 10^{-3} \\ -10^{-4} & \delta U^t < 10^{-5} \end{cases}$$

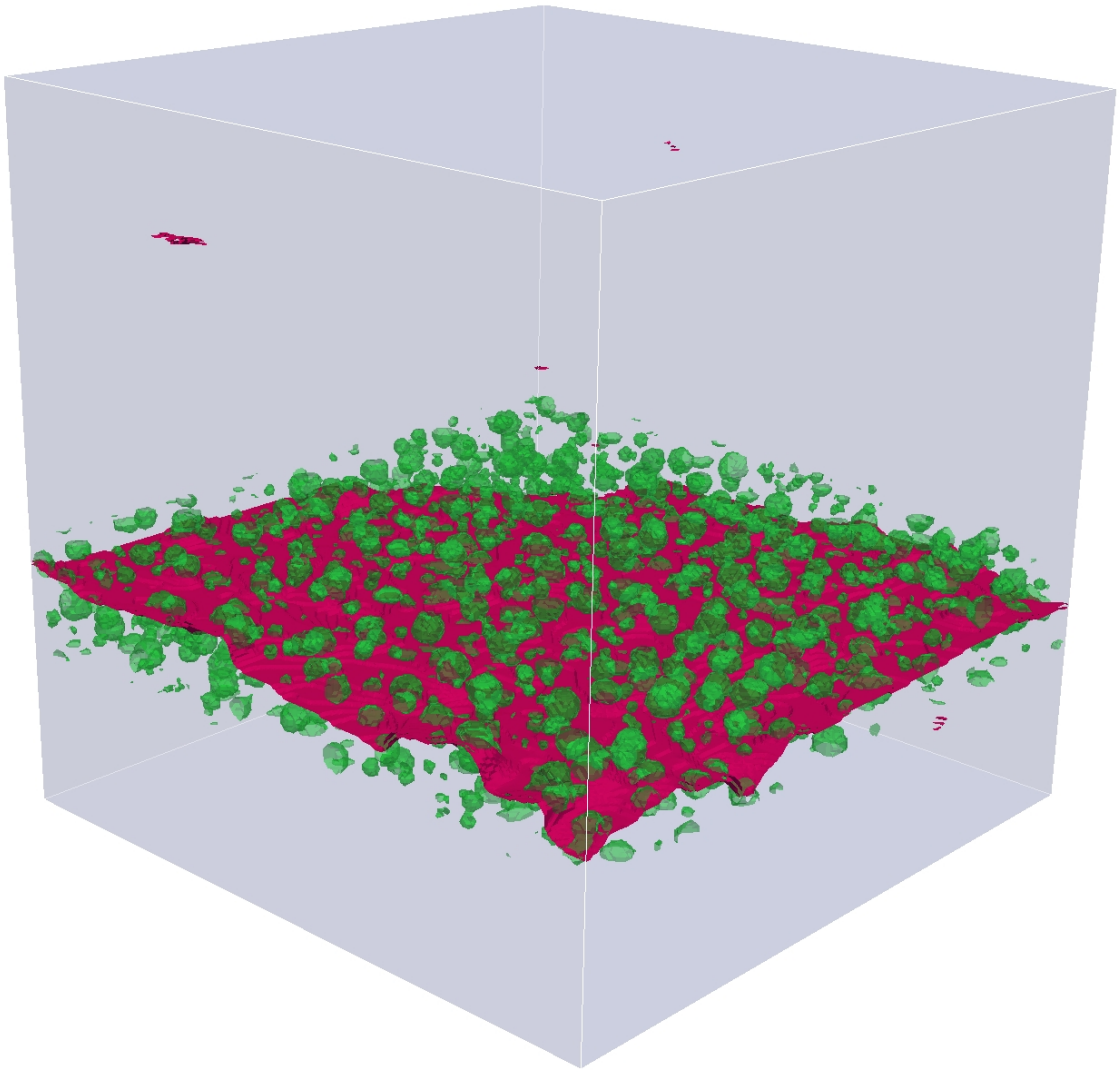

Figure 20: Crack surface in cast iron at $t = 2390$

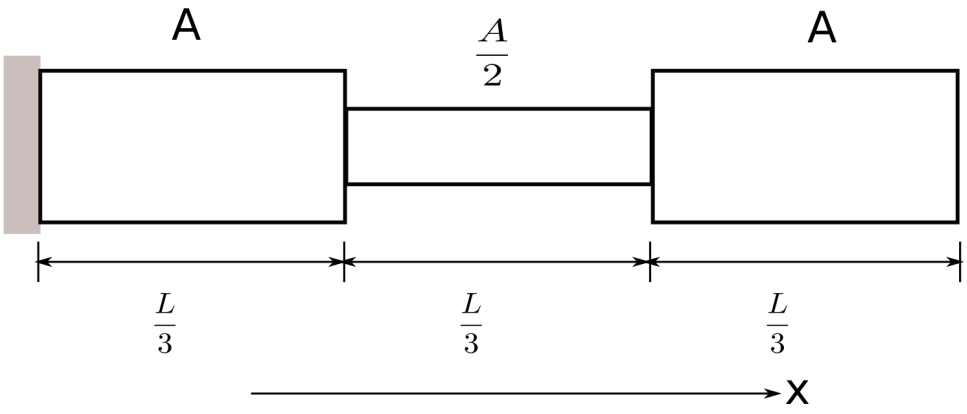

Figure 21: Bar of length L with a reduced cross section in the center

for $\delta U^t < 0$

$$\delta U^{t+1} = \begin{cases} 0.001\delta U^t & \delta d_{max} < 0.001 \\ \delta U^t & 0.001 \leq \delta d_{max} \leq 0.00125 \\ 2\delta U^t & \delta d_{max} > 0.00125 \\ -10^{-3} & \delta U^t < -10^{-3} \\ 10^{-5} & \delta U^t > -10^{-5} \end{cases}$$

with $\delta U^t = 10^{-3}$ at the first time step.

The distribution of d along the bar at $d_{max} = 0.99$ is presented in Figure 22. The load–displacement curve is also obtained (see Figure 23). These two figures show that the result obtained by our strategy is similar to [35]. A small difference for the maximum load can be marked and also for the shape of d. However, note that different crack density functions are used in this paper and their work.

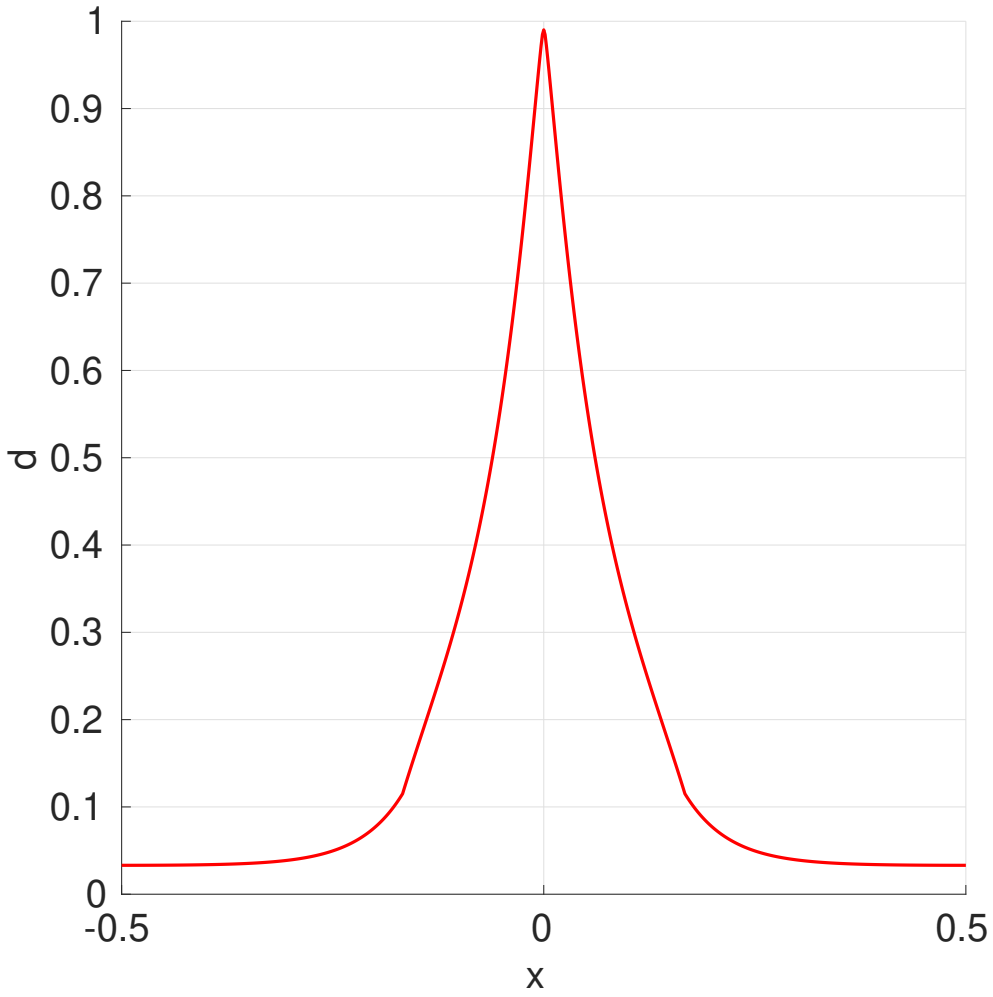

Figure 22: Distribution of the phase field parameter d along the bar at $d_{max} = 0.99$

Data availability

The raw/processed data required to reproduce these findings cannot be shared at this time as the data also forms part of an ongoing study.

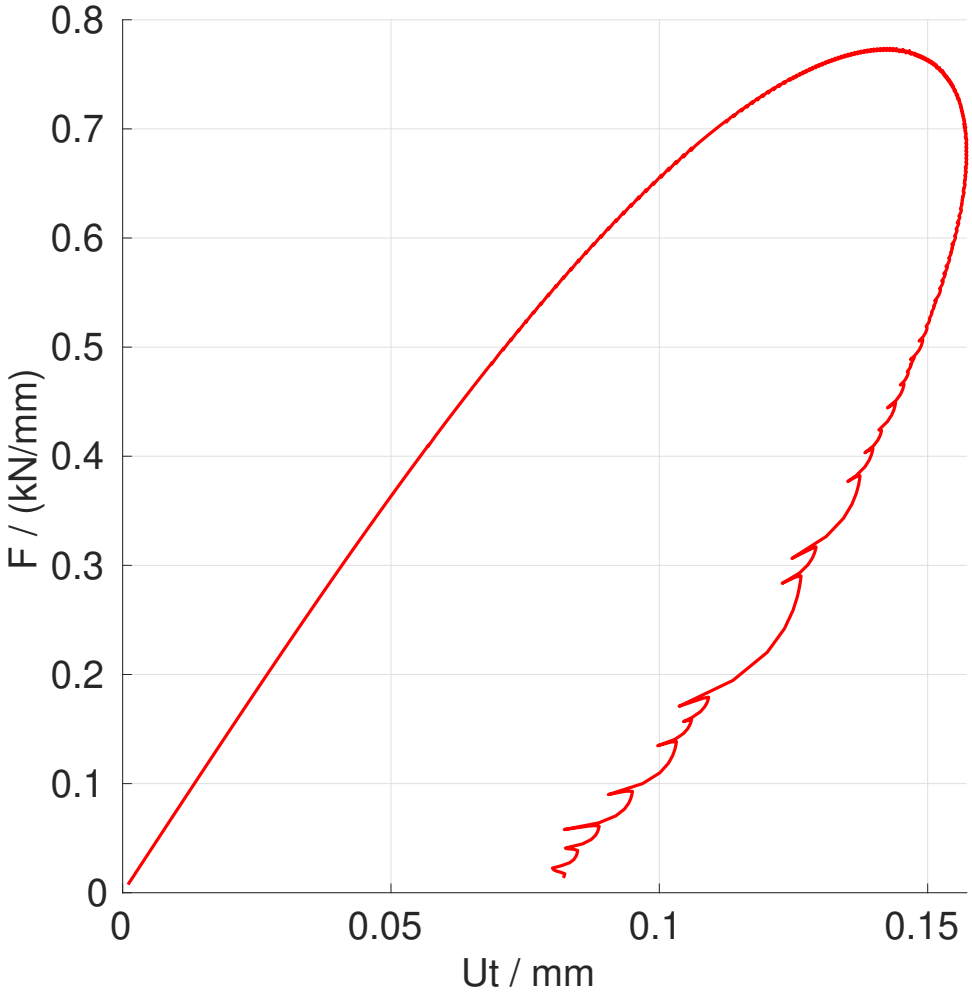

Figure 23: Load – displacement curves for $d_{max} = 0.99$

References

References

[1] B. P. Flannery, H. W. Deckman, W. G. Roberge, K. L. D'AMICO, Three-dimensional x-ray microtomography, Science 237 (4821) (1987) 1439–1444.

[2] J. Rannou, N. Limodin, J. Réthoré, A. Gravouil, W. Ludwig, M.-C. Baïetto-Dubourg, J.-Y. Buffiere, A. Combescure, F. Hild, S. Roux, Three dimensional experimental and numerical multiscale analysis of a fatigue crack, Computer methods in applied mechanics and engineering 199 (21-22) (2010) 1307–1325.

[3] P. Lecomte-Grosbras, B. Paluch, M. Brieu, G. De Saxcé, L. Sabatier, Interlaminar shear strain measurement on angle-ply laminate free edge using digital image correlation, Composites Part A: Applied Science and Manufacturing 40 (12) (2009) 1911–1920.

[4] B. Bourdin, G. A. Francfort, J.-J. Marigo, Numerical experiments in revisited brittle fracture, Journal of the Mechanics and Physics of Solids 48 (4) (2000) 797–826.

[5] G. A. Francfort, J.-J. Marigo, Revisiting brittle fracture as an energy minimization problem, Journal of the Mechanics and Physics of Solids 46 (8) (1998) 1319–1342.

[6] A. Griffith, The theory of rupture, in: First Int. Cong. Appl. Mech, 1924, pp. 55–63.

[7] T. T. Nguyen, J. Yvonnet, Q.-Z. Zhu, M. Bornert, C. Chateau, A phase field method to simulate crack nucleation and propagation in strongly heterogeneous materials from direct imaging of their microstructure, Engineering Fracture Mechanics 139 (2015) 18–39.

[8] T. T. Nguyen, J. Réthoré, M.-C. Baietto, Phase field modelling of anisotropic crack propagation, European Journal of Mechanics-A/Solids 65 (2017) 279–288.

[9] T.-T. Nguyen, J. Réthoré, J. Yvonnet, M.-C. Baietto, Multi-phase-field modeling of anisotropic crack propagation for polycrystalline materials, Computational Mechanics 60 (2) (2017) 289–314.

[10] G. Molnár, A. Gravouil, 2d and 3d abaqus implementation of a robust staggered phase-field solution for modeling brittle fracture, Finite Elements in Analysis and Design 130 (2017) 27–38.

[11] P. Zhang, X. Hu, T. Q. Bui, W. Yao, Phase field modeling of fracture in fiber reinforced composite laminate, International Journal of Mechanical Sciences 161 (2019) 105008.

[12] T. Noll, C. Kuhn, D. Olesch, R. Müller, 3d phase field simulations of ductile fracture, GAMM-Mitteilungen 43 (2) (2020) e202000008.

[13] N. Nguyen-Thanh, W. Li, J. Huang, K. Zhou, Adaptive higher-order phase-field modeling of anisotropic brittle fracture in 3d polycrystalline materials, Computer Methods in Applied Mechanics and Engineering 372 (2020) 113434.

[14] E. Eid, R. Seghir, J. Réthoré, Multiscale analysis of brittle failure in heterogeneous materials, Journal of the Mechanics and Physics of Solids 146 (2021) 104204.

[15] S. Riad, D. Bardel, J. Réthoré, Unified phase field model to simulate both intergranular and transgranular failure in polycrystalline aggregates, Finite Elements in Analysis and Design 194 (2021) 103555.

[16] C. Miehe, F. Welschinger, M. Hofacker, Thermodynamically consistent phase-field models of fracture: Variational principles and multi-field fe implementations, International journal for numerical methods in engineering 83 (10) (2010) 1273–1311.

[17] T. T. Nguyen, J. Yvonnet, M. Bornert, C. Chateau, Initiation and propagation of complex 3d networks of cracks in heterogeneous quasi-brittle materials: Direct comparison between in situ testing-microct experiments and phase field simulations, Journal of the Mechanics and Physics of Solids 95 (2016) 320–350.

[18] T. T. Nguyen, J. Yvonnet, M. Bornert, C. Chateau, F. Bilteryst, E. Steib, Large-scale simulations of quasi-brittle microcracking in realistic highly heterogeneous microstructures obtained from micro ct imaging, Extreme mechanics letters 17 (2017) 50–55.

[19] S. Lee, M. F. Wheeler, T. Wick, Pressure and fluid-driven fracture propagation in porous media using an adaptive finite element phase field model, Computer Methods in Applied Mechanics and Engineering 305 (2016) 111–132.

[20] T. Heister, T. Wick, Parallel solution, adaptivity, computational convergence, and open-source code of 2d and 3d pressurized phase-field fracture problems, Pamm 18 (1) (2018) e201800353.

[21] X. Liu, J. Réthoré, M.-C. Baietto, P. Sainsot, A. A. Lubrecht, An efficient strategy for large scale 3d simulation of heterogeneous materials to predict effective thermal conductivity, Computational materials science 166 (2019) 265–275.

[22] X. Liu, J. Réthoré, M.-C. Baietto, P. Sainsot, A. A. Lubrecht, An efficient finite element based multigrid method for simulations of the mechanical behavior of heterogeneous materials using ct images, Computational Mechanics 66 (6) (2020) 1427–1441.

[23] R. E. Bank, C. C. Douglas, Sharp estimates for multigrid rates of convergence with general smoothing and acceleration, SIAM journal on numerical analysis 22 (4) (1985) 617–633.

[24] R. Kettler, J. Meijerink, A multigrid method and a combined multigrid-conjugate gradient method for elliptic problems with strongly discontinuous coefficients in general domains.

[25] R. Kettler, Analysis and comparison of relaxation schemes in robust multigrid and preconditioned conjugate gradient methods, in: Multigrid methods, Springer, 1982, pp. 502–534.

[26] O. Tatebe, The multigrid preconditioned conjugate gradient method, in: NASA conference publication, NASA, 1993, pp. 621–621.

[27] S. F. Ashby, R. D. Falgout, A parallel multigrid preconditioned conjugate gradient algorithm for groundwater flow simulations, Nuclear science and engineering 124 (1) (1996) 145–159.

[28] L. Gilles, C. R. Vogel, B. L. Ellerbroek, Multigrid preconditioned conjugate-gradient method for large-scale wave-front reconstruction, JOSA A 19 (9) (2002) 1817–1822.

[29] J. D. Wilson, R. L. Naff, Multigrid preconditioned conjugate-gradient solver for mixed finite-element method, Computational Geosciences 14 (2) (2010) 289–299.

[30] D. Braess, On the combination of the multigrid method and conjugate gradients, in: Multigrid methods II, Springer, 1986, pp. 52–64.

[31] A. A. Griffith, Vi. the phenomena of rupture and flow in solids, Philosophical transactions of the royal society of london. Series A, containing papers of a mathematical or physical character 221 (582-593) (1921) 163–198.

[32] H. Amor, J.-J. Marigo, C. Maurini, Regularized formulation of the variational brittle fracture with unilateral contact: Numerical experiments, Journal of the Mechanics and Physics of Solids 57 (8) (2009) 1209–1229.

[33] M. A. Gutiérrez, Energy release control for numerical simulations of failure in quasi-brittle solids, Communications in Numerical Methods in Engineering 20 (1) (2004) 19–29.

[34] C. V. Verhoosel, J. J. Remmers, M. A. Gutiérrez, A dissipation-based arc-length method for robust simulation of brittle and ductile failure, International journal for numerical methods in engineering 77 (9) (2009) 1290–1321.

[35] T. Linse, P. Hennig, M. Kästner, R. de Borst, A convergence study of phase-field models for brittle fracture, Engineering Fracture Mechanics 184 (2017) 307–318.